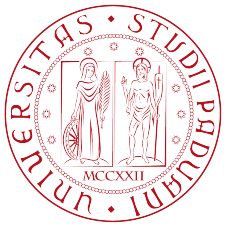

UNIVERSITÀ DEGLI STUDI DI PADOVA

Dipartimento di Fisica e Astronomia "Galileo Galilei"

Corso di Laurea Magistrale in Fisica

Studies for a proton tomography scanner

Relatore:
Prof. Piero Giubilato

Correlatore:
Dott. Nicola Pozzobon

Laureando:
Filippo Baruffaldi
Matricola: 1127983

Controrelatore:
Prof. Francesco Recchia

Anno Accademico 2016/2017

Contents

1 Introduction

iMPACT, *innovative Medical Proton Achromatic Calorimeter and Tracker*, is a University of Padova and INFN project, funded by the *European Research Council*. The project aim is to design, develop and prototype an extremely fast and accurate *proton Computed Tomography Scanner*, with the ultimate goal of enabling the realization of a clinically viable proton Computed Tomography (pCT) system. Proton Computed Tomography is an extremely promising technique able to reconstruct density maps (images) of the human body with minimal dose release and high tissue density accuracy, a particularly critical feature in cancer *hadron-therapy* treatment planning. Hadron-therapy is a leading edge technique where protons or heavy-ions, instead of X-rays, are used to target and destroy the tumor within the human body. By exploiting the peculiar energy deposition distribution such highly ionizing, heavy particles exhibit, it is in fact possible to confine within a volume of few mm^3 most of the energy released, hence sparing the healthy tissues surrounding the tumor.
However, despite all its beneficial aspects, hadron-therapy is not yet widespread as other more established procedures, such as X-ray therapy. One of the reasons is that the current X-ray Computed Tomography (X-ray CT), currently used to produce body density maps, cannot deliver maps accurate enough to exploit the intrinsic accuracy of the hadron treatment. To precisely aim the hadron energy release with millimeter precision, it is in fact necessary to possess very accurate knowledge of the density it traverse before reaching the tumor. The idea standing behind the development of a pCT scanner is that using the same energy loss behaviour for both the imaging process and the treatment would improve the performance of the latter, the physical interaction process being the same. Currently, several pCT scanner prototypes are being developed around the world; pCT scanner technology however is still far from being applicable in a clinical environment, mainly due to the slow acquisition rates. The iMPACT project therefore plans to develop a pCT scanner able to overcome such limitations, leading the way toward medically sound apparatuses.
This thesis work begins by displaying both limitations and advantages of the hadron-therapy technique; the pCT state-of-the-art is then reviewed, highlighting positive features as well as constraints that limit its applicability. The current state of the iMPACT scanner, which embeds a tracker system and a calorimeter, is illustrated and discussed. The thesis then focuses on the development of the calorimeter part of the scanner. The development of a Monte Carlo simulation is presented together with a calibration procedure based on data collected at proton beam tests. Additional studies with proton data are presented with an outlook on future developments.

2 Hadron-Therapy

2.1 Protons and hadrons in cancer treatment

In present days, tumors are the main cause of death in developed countries and the second one in developing countries [1]. Currently the most used medical procedures to cure these tumors consist in surgery, chemotherapy and X-ray therapy, with the latter used in more than 40% of the patients affected by localized malignant tumors [2, 3].
X-ray therapy relies on using MeV-scale photons to deliver ionizing radiation dose in organic tissues; the deposited energy can damage the molecules inside cells, including the DNA, therefore hindering cellular reproduction. In the ideal case the tumor volume is treated with the exact dose necessary to eliminate all the cancerous cells, avoiding at the same time energy deposition in the surrounding healthy tissues.
As can be seen in Fig. 1, however, the photon dose-depth profile reaches its maximum a few cm under the surface, decreasing exponentially afterwards, due to photons absorption in the material. This behaviour impairs the capability to accurately target a limited volume without significantly affecting surrounding tissues, being this a particularly constraining limit in case of deep-seated tumors treatment. X-ray treatments are often supplied targeting the tumor from multiple directions, to spread the non necessary dose over a larger volume.
In Fig. 1 the dose-depth profile of protons (blue curve) and carbon ions (red curve) is also shown, according to the Bethe-Bloch formula, Eq. 4. For both protons and ^{12}C the energy loss is inversely proportional to the square of their velocity, so the energy deposition presents a sharp maximum, known as Bragg peak, located close to the end of the particle path, while the energy deposition before the peak is rather low (about 20% of the maximum) and almost absent after the peak. The depth can be adjusted to precisely match the tumor position by changing the initial energy of the particles. The cancer treatment that relies on ion beams (principally ^{12}C) is called hadrontherapy, or protontherapy if limited to protons.

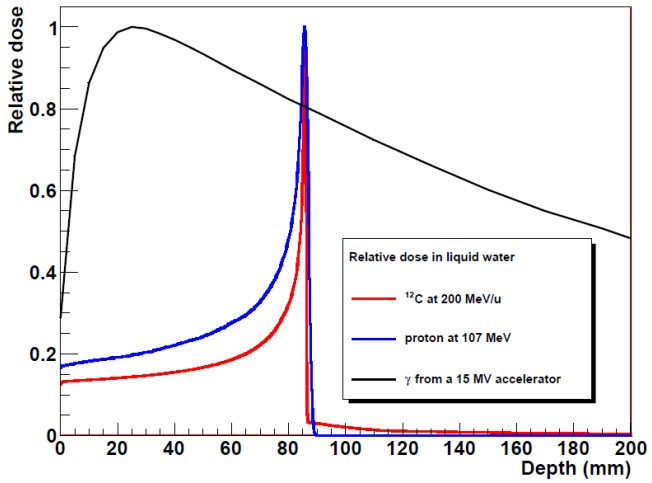

Fig. 1: Comparison of the dose depth profile in water for carbon ions, protons and X-rays [3].

To uniformly cover a larger area (a process called tumor painting), protons or heavier ions with different energies are used: the energies and the intensity of several beams are calibrated so that the total dose deposited presents a plateau covering the volume of the tumor; this constant dose profile is called Spread Out Bragg peak, or SOBP, as shown in Fig. 2. In this case the fraction of the dose deposited before the SOBP is higher in respect with the single energy Bragg peak (up to 50% of the maximum), depending on the number of beams used to paint the volume.

Fig. 3 shows a comparison of the planned dose map optimized to paint a tumor located close to the center of a human head, with either photons or protons. While the largest fraction of the photon beam is absorbed before reaching the tumor depth, damaging primarily healthy tissues instead of the tumor itself, on the other hand a proton SOBP covers mainly the planned volume, causing a low dose deposition in front of the tumor and leaving the volume behind the peak almost unaffected, a particularly favorable characteristic in case of proximity of organs at risk, such as brain or spinal tissues. In real treatments the beam is aimed at the tumor from many different angles over a 180° span, further improving the benefits of the painting technique.

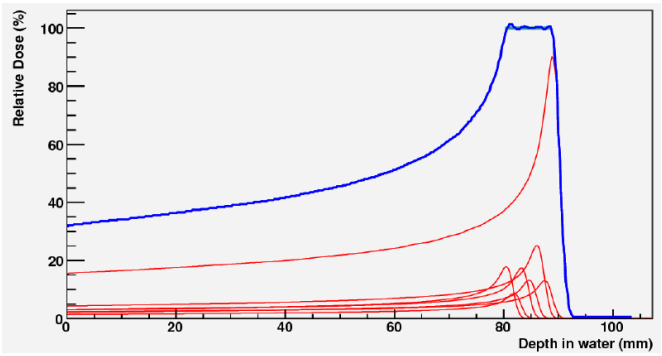

Fig. 2: Tumor painting concept: several proton beams with different energies (red) are summed up to form the so-called Spread Out Bragg peak (blue) [3].

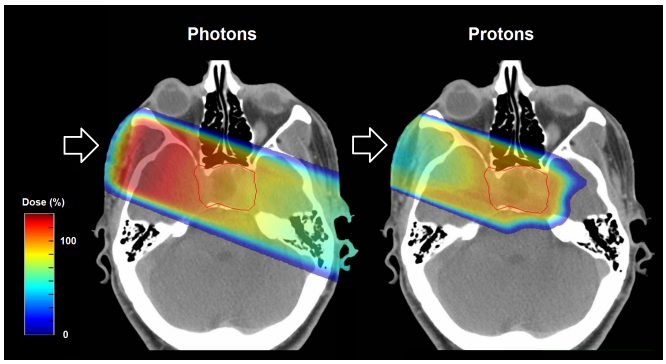

Fig. 3: Software-planned dose map on a human head in case of treatment with photons (left) or protons (right) [4].

Robert Wilson was the first to suggest the use of proton beams in medical therapy, back in 1946 [5]: two years later studies begun on the physical and biological properties of proton using the 184 inches synchrocyclotron at Lawrence Berkeley Laboratory (USA) [6]. Between 1954 and 1975 about 1000 patients were treated in Berkeley, using protons and heavier ions, mainly ^{20}Ne. Between 1975 and 1993 medical irradiations with ^{20}Ne and ^{12}C beams were administered at the Massachusetts General Hospital. In 1994 the Heavy Ion Medical Accelerator (HIMAC) was built at the National Institute of Radiological Science in Chiba (Japan), dedicated to carbon beam therapy.
Nowadays, up to 65 centers are operating for both protons and carbon ions and more than 50 facilities are in realization or planning phase, mainly in Japan, China, USA and European countries [7, 8]. At the end of 2013, a total of 105,743 patients have been treated with protons only, and 13,552 with heavier ions [9]. Fig. 4 shows the growth during the last decades of the number of hadron-therapy centers and treated patients.

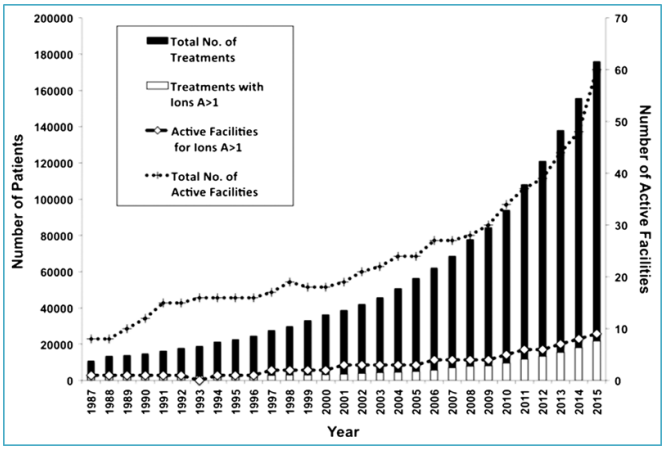

Fig. 4: Number of active hadron therapy facilities and treated patients, from 1987 to 2015. The number of facilities providing heavier-than-proton ion beams and the corresponding patient population are highlighted [10].

2.2 Relative biological effectiveness and oxygen enhancement ratio

Beyond the dose depth-profile characterized by the Bragg peak, another advantageous feature of protons and ions over photons is their biological effectiveness, described by the relative biological efficiency factor (RBE). The RBE is defined as the ratio between the dose deposited by photons D_{phot} in respect with dose deposited by a given hadron D_{hadr} in order to cause the same damage to the biological tissue:

$$\text{RBE} = \frac{D_{\text{phot}}}{D_{\text{hadr}}} \tag{1}$$

where the biological damage is evaluated by the fraction S of the number of cells that survive after the deposition of a dose D; dose is defined as the absorbed energy per unit mass and in the SI is measured in Gray (Gy), 1 Gray = 1 J/kg. The survival fraction S can be parametrized by a linear-quadratic model:

$$S(D) = \exp(-\alpha D - \beta D^2) \tag{2}$$

where α and β are experimental determined parameters [11]. Fig. 5 shows the survival fraction as a function of the dose for photons and a generic ion. Values of the RBE are around $1.5 - 2.1$, meaning that hadrons require an appreciably lower dose than photons to produce the same biological effect. Ions with higher masses have usually higher RBE values, for example carbon reaches a RBE of ≈ 3, and therefore are more effective than lighter ions, such as protons.
Another parameter affecting the efficiency of the treatment is the oxygen concentration: cells with low oxygen content (hypoxic) are generally more radiation resistant than cells with normal oxygenation (aerobic), so a higher dose is needed to kill them. Unfortunately the cancer cells are generally hypoxic, due to their abnormal growth rate and oxygen consumption. The Oxygen Enhancement Ratio (OER) is defined as:

$$\text{OER} = \frac{D_{\text{hypoxic}}}{D_{\text{aerobic}}} \tag{3}$$

where D_{hypoxic} and D_{aerobic} is the dose required to have the same survival fraction on hypoxic and aerobic cells respectively. OER varies for different particles and depends on the linear

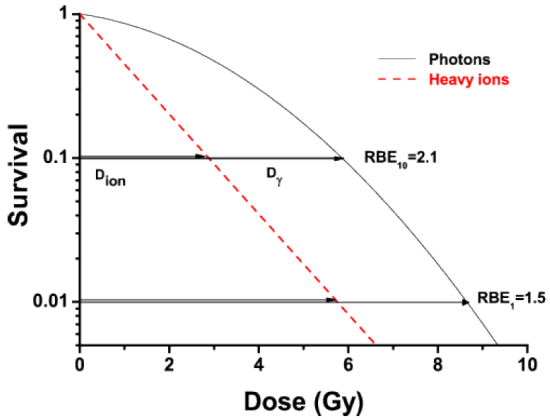

Fig. 5: Survival fraction as a function of dose for photons and a generic ion. RBE is indicated for 10% and 1% survival levels [2].

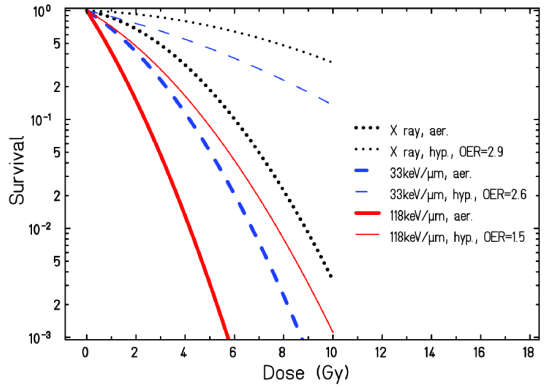

Fig. 6: Influence of the oxygen level on cell survival of human kidney cells for carbon ions with different LET [2].

energy transfer (LET, the deposited energy per unit length, usually misured in keV/µm) of the particle. Fig. 6 shows the survival fraction as a function of the dose for photons and carbon ions with different LET values. X-rays have OER around 3, while protons and other ions present lower OER: high LET ^{12}C ions result in an OER $\approx$ 2, while ions heavier than ^{20}Ne reach an OER of about 1. Accordingly, hadrons proved to be more effective than photons for the treatment of hypoxic cells, such as tumoral ones.

2.3 Proton range and range straggling

Protons travel along a roughly straight line through matter, continuously losing energy by Coulomb inelastic interactions with atomic electrons; to a first order approximation the electron mass is in fact too low to make a substantial change to the proton direction. Protons also interact via Coulomb elastic scattering with the positive-charged atomic nuclei, which can deflect the particle trajectory (the deflection angle probability is described by Rutherford's relation Eq. (12)). Nuclear scattering is also possible but less frequent (around 15% of 200 MeV protons undergo nuclear inelastic reactions along their path [3]); in this case a proton overcomes the Coulomb nuclear barrier, interacting inelastically with the atomic nucleus; the reaction can produce neutrons, secondary protons, γ-rays or light ions. The secondary protons produced via nuclear interactions are responsible of about 10% of the total dose deposited by

a 200 MeV proton beam [12].
The mean energy loss rate per unit length, or Stopping Power S_p ($S_p = -\text{LET}$), of a projectile particle in a material via Coulomb interactions with electrons can be described by the Bethe and Bloch formula [13, 14], a quantum-mechanical extension of the Bohr calculation [15]):

$$S_p = -\left\langle \frac{dE}{dx} \right\rangle = \frac{4\pi}{m_e c^2} \cdot \frac{nz^2}{\beta^2} \cdot \left(\frac{e^2}{4\pi\varepsilon_0} \right)^2 \cdot \left[\ln\left(\frac{2m_e c^2 \beta^2}{I \cdot (1-\beta^2)} \right) - \beta^2 - \frac{\delta}{2} - \frac{C}{Z} \right] \tag{4}$$

where m_e is the electron mass, β is the projectile speed in units of c, z is the the projectile electric charge, I is the mean excitation potential of the material, δ is the outer electrons shielding correction, C is a shell-correction parameter and the electron density n can be calculated with:

$$n = \frac{N_A \cdot Z \cdot \rho}{A \cdot M_u} \tag{5}$$

where N_A is the Avogadro number, Z and A are the material atomic and mass number respectively, ρ is the mass density of the absorbing material and $M_u = 1$ g/mol. At low particle speed, namely $E < 10$ MeV/u, the particle charge has to be substituted by an effective charge Z_{eff} [16]:

$$z \to z_{\text{eff}} = z \left[1 - \exp\left(-125\beta z^{-\frac{2}{3}} \right) \right] \tag{6}$$

to take into account the decrease of mean projectile particle charge due to ionization and recombination processes.
Equation (4) shows how the stopping power is strictly related to the absorbing material properties, most strongly on the material density. In fact, the factor Z/A varies less than 20% for biologic materials; the dependence on the excitation potential is logarithmic, with I varying from 19 eV for ^{1}H to 820 eV for ^{208}Pb; energy loss is instead proportional to the mass density, whose values in a human body can cover a range of three orders of magnitude, from air in the lung (0.0012 g/cm^3) to cortical bone (up to 2 g/cm^3). It is clear that precisely knowing the tissues density distribution is essential to plan a proton-therapy treatment with sufficient accuracy [12].
The projectile mean range, as shown in Fig. 7, is defined as the depth in a material at which, on average, half the particles have stopped; in some cases only particles arriving near the end of the path are taken into account, neglecting those removed via nuclear reactions.

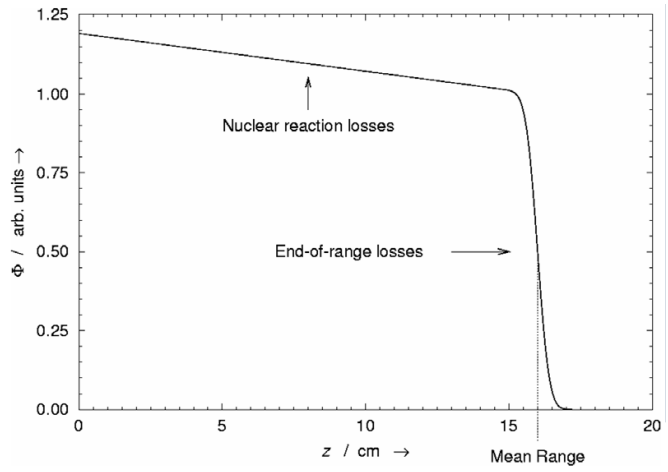

Fig. 7: Fluence Φ of a proton beam in water as a function of depth z, normalized to 1 near the end of the path [12].

Considering the particles path strictly linear, therefore neglecting lateral scattering, the range of a monoenergetic beam can be expressed as:

$$R(E) = \int_0^E \left\langle \frac{dE'}{dx} \right\rangle^{-1} dE' \tag{7}$$

where E is the energy of the beam; considering a linear path is an acceptable approximation in most clinical situations, where the proton range typically spans between 1 mm (the typical voxel size in medical imaging) to about 30 cm (the deepest site in the human body) [12].
Bragg and Kleeman, in 1905, identified an analytical expression that puts the particle range in relation with its energy, for a given absorber material [17]:

$$R(E) = \alpha E^p \tag{8}$$

where α and p are absorber and particle dependent parameters derived experimentally [18, 19]. The energy-range relation is shown in Fig. 8 for typical ions used in hadrontherapy.

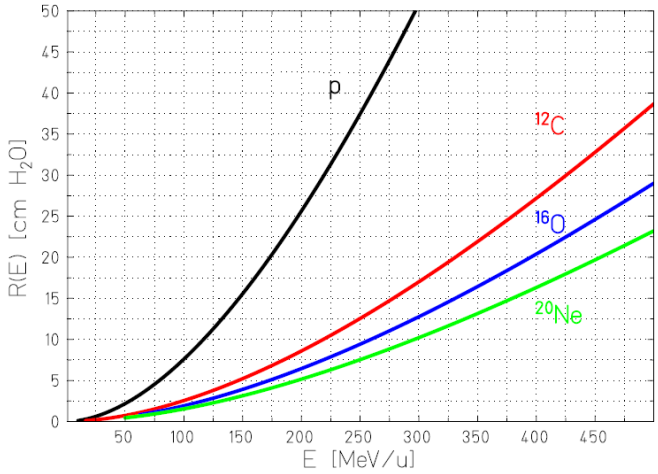

Fig. 8: Simulated range in water of different particles as a function of energy [2].

Range describes an average behaviour, while the stochastic nature of the single inelastic Coulomb scattering, integrated over a wide number of collisions, leads to statistical fluctuations of the energy loss rate, called energy straggling. This dispersion causes a spread of the particles range around its mean value (range straggling) and therefore a broadening of the Bragg peak.
The energy loss ΔE of a particle passing through a layer of material is distributed according to a probability density function $f(\Delta E)$. This distribution was described by Vavilov [20] for thin layers and Landau [21] for intermediate thickness layers; however in the limit of many collisions (thick layers) the Vavilov and Landau asymmetric distributions can be approximated by a gaussian with a mean value $\langle \Delta E \rangle$ and a variance $(\sigma_E^{\text{stragg}})^2$, given by:

$$(\sigma_E^{\text{stragg}})^2 = 4\pi z_{\text{eff}} Z e^4 n \Delta x \left[\frac{1 - \beta^2/2}{1 - \beta^2} \right] \tag{9}$$

where n is the electron density, defined in Eq. (5), and Δx the layer thickness (Bohr [22, 23]).
Range straggling is related to energy straggling by the expression:

$$(\sigma_R^{\text{stragg}})^2 = \int_0^E \left(\frac{d\sigma_{E'}^{\text{stragg}}}{dx} \right) \left(\frac{dE'}{dx} \right)^{-3} dE' \tag{10}$$

The ratio between range straggling and range can be shown to be energy dependent (B. Rossi [24]), and described by:

$$\frac{\sigma_R^{\text{stragg}}}{R} = f\frac{1}{\sqrt{m}}\left(\frac{E}{mc^2}\right) \tag{11}$$

where m is the particle mass and f is a slowly varying function depending on the absorber. The $1/\sqrt{m}$ dependence makes the relative range straggling smaller for heavier ions; e.g. for ^{12}C the relative range straggling is a factor 3.5 smaller with respect to protons [2].
Experimental values of range and range straggling for protons with varying energies in different materials have been measured and tabulated by J. Janni [25]; for $\sim$ 200 MeV protons the relative range straggling σ_R^{stragg} stands between 0.9 and 1.2%. The range straggling establish an intrinsic limit to the precision with which particle ranges can be predicted and measured.

2.4 Lateral dispersion

Protons and ions passing close to a nucleus are deflected by Coulombian interaction, as described by Rutherford's theory [26]. The differential cross section of a single scattering is:

$$\frac{d\sigma}{d\Omega} = z^2 Z^2 r_e^2 \left(\frac{m_e c}{4\beta p}\right)^2 \sin^{-4}\left(\frac{\theta}{2}\right) \tag{12}$$

where θ is the scattering angle, Ω is the solid angle, r_e is the classical electron radius and p is the particle momentum, therefore small deflections are much favored.
In a typical clinical case the thickness of the absorber is high enough so that the single scattering limit is no longer acceptable. A complex Multiple Coulomb Scattering (MCS) theory was proposed by Molière in 1948 [27], expressing the statistical distribution $F(\theta_{\text{tot}}, d)$ of the total resulting scattering angle θ_{tot} at depth d with an analytical solution; however, for small angles, the Molière's solution can be approximated by a gaussian distribution with a standard deviation given by [28]:

$$\sigma_\theta = \frac{1.41\text{MeV}}{\beta pc} z\sqrt{\frac{d}{L_{\text{rad}}}}\left[1 + \frac{1}{9}\log_{10}\left(\frac{d}{L_{\text{rad}}}\right)\right] \tag{13}$$

where L_{rad} is the material radiation length, whose values can be found tabulated in [29] (for example L_{rad} for water is 36.8 g/cm^2). For a given thickness, higher density materials cause a wider angular spread, while protons are deflected more than heavier ions by the same amount of material. A 200 MeV proton beam in water, with an initial FWHM$= \sigma_\theta\sqrt{2\ln 2} \approx 0.7$ cm, can be broadened by MCS up to 1.6 cm in close proximity to the Bragg peak, as shown in Fig. 9.

2.5 Proton Tomography

The effectiveness of a proton-therapy treatment is strictly related to the accuracy of the treatment planning, which requires a good knowledge of the body stopping power map: knowing the 3D distribution of the tissues stopping power makes it possible to precisely determine the position of the Bragg peak as a function of the particle energy.
Currently, the treatment planning for both photon and proton-therapy is based on 3D maps taken with the X-ray Computed Tomography (X-ray CT): a rotating photon beam invests the scanned object, while a detector positioned on the opposite side measures the intensity of the beam, producing a 2D absorption map for each imaging angle. The data are then analyzed with a reconstruction software, which eventually provides a Hounsfield units 3D map [30]. Hounsfield units (HU) are defined as:

$$\text{HU} = 1000 \cdot \left(\frac{\mu - \mu_{\text{water}}}{\mu_{\text{water}} - \mu_{\text{air}}}\right) \tag{14}$$

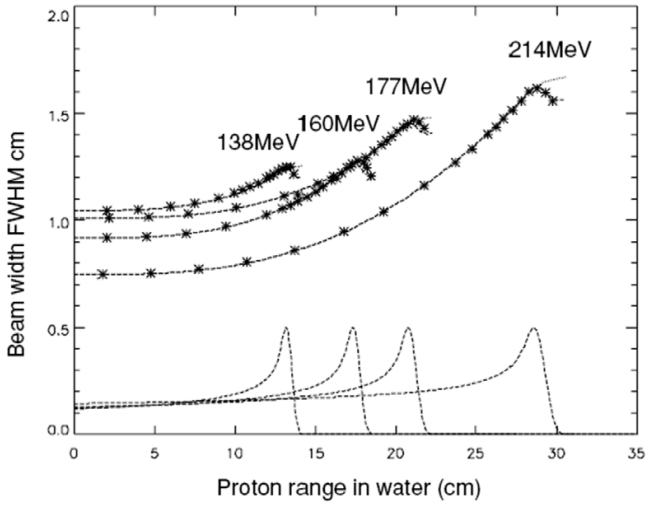

Fig. 9: Lateral dispersion of a proton beam with different energies, in water; corresponding Bragg peak positions are superimposed [12].

where μ is the average linear attenuation coefficient in a given position inside the object, μ_{water} and μ_{air} are the water and air attenuation coefficients.
A calibration curve, obtained from known materials, is then used to estimate the electron density from the HU map. While the 3D HU map is perfect to correctly tune the X-ray delivery, for proton-therapy, an equivalent Stopping Power map must be extrapolated. Often the Stopping Power of a given material ${S_p}^{\text{material}}$ is expressed in terms of the relative stopping power RSP:

$$\text{RSP} = \frac{{S_p}^{\text{material}}}{{S_p}^{\text{water}}} \tag{15}$$

where ${S_p}^{\text{water}}$ is the stopping power in water.
Different approaches, both theoretical [31] and experimental [32], where explored to correlate HU and RSP values, obtaining uncertainties on the proton range around 5% and 2% respectively, which are, at best, as large as twice the intrinsic theoretical limit of 1%, given by the range straggling. The main obstacle is the different dependence of HU and RSP on Z and Z/A, which produce a non univocal correlation between them [30].
A determination of RSP directly from proton energy loss measurements, bypassing the HU-RSP conversion, would therefore provide a more accurate proton range prevision and eventually a more effective treatment plan, since the same particle is used for both imaging and treatment. The procedure consisting in using protons for imaging purposes is known as proton Computed Tomography, or pCT.
A. Corkmack in 1963 was the first to propose the usage of charged-particles energy loss measurements to determine the 2D stopping power distribution of an object [33, 34], and also realized the potential radiological applications of the method. The first 3D recontruction was performed in 1972 by Goitein, from alpha particle energy loss information [35]. Two years later Corkmack and Koehler performed the first studies on the usage of protons for 3D density reconstructions [36].
In 2004 a study (U. Schneider et al. [37]) found the RSP values accuracy to be potentially a factor 2.5 better for pCT with respect to X-ray CT. The same study proved the pCT to be advantageous on a dosimetric perspective, with at least a factor 50 lower deposited dose than X-ray CT in order to obtain comparable density resolutions. However the spatial resolution is expected to be worse for pCT than X-ray CT, mostly due to protons multiple Coulomb scattering [38].

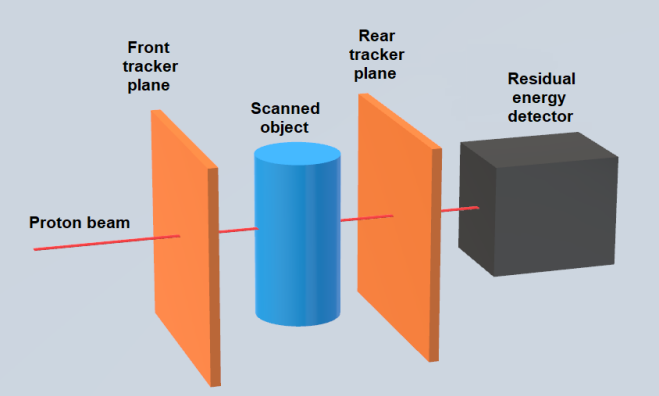

Fig. 10: Schematic representation of typical pCT scanner layout.

Nowadays several pCT scanner prototypes are being studied around the world, mainly in USA, Europe and Japan: a list of current pCT projects is presented in Tab. 1. All the existing setups share very similar layouts, represented in Fig. 10: a proton tracking system coupled with a proton residual energy detector [30]. Every pCT scanner prototype is designed in a way that foresees the possibility for the entire apparatus to mechanically rotate around the scanned object, given the impossibility to move the patient maintaining the relative position of the internal tissues. The tracking system includes a front plane, placed before the scanned object and a rear plane placed after the object, to reveal entering and exiting proton positions and directions. The residual energy of each proton is then measured; the RSP map is eventually computed combining the measurements of energy and tracking of every single protons.
For tracking purposes, current prototypes use either position sensitive x-y Silicon Strip Detectors (SSD) planes or x-y Scintillating Fiber (Sci-Fi) planes (Tab. 1). Both SSD and Sci-Fi are one dimensional detectors, arranged in x and y planes alternatively, in order to retrieve the two dimensional proton coordinates.
The residual energy is almost exclusively measured with scintillators calorimeters, for their fast response and possibility to cover large volumes, with the exception of the PRaVDA collaboration, which uses solid-state detectors [39].
Different algorithms and softwares are being developed for the object 3D image reconstruction from the tracks-energy information. These algorithms are based on the Most Likelihood Path (MLP) formalism, which uses the initial and final proton tracks to evaluate the most likely proton path inside the object, taking into account the multiple Coulomb scattering. An example of a MLP proton track reconstruction is presented in Fig. 11, where a Monte Carlo simulated proton track in water is compared with its relative software reconstruction [40]. The MLP reconstruction provides a smooth path, averaging multiple small-angle scattering. A number of about 10^9 recorded proton tracks-energies is required to have a pCT imaging quality comparable to a standard X-ray CT [41]. Once the most likely paths of an adequate number of protons are obtained, the 3D RSP map can be produced with the Algebraic Reconstruction Technique (ART), an iterative method that starts from an arbitrary initial image, even a blank picture, and combines the path-energy loss information into a more refined image in each consecutive step (a complete explanation can be found in [42]).

2.6 Present limitations of proton tomography

Proton Tomography techniques have not become clinically viable technologies yet, as opposed to the widely established X-ray CT technique, due to physical, experimental and accessibility limitations. A relevant physical limitation is given by the multiple Coulomb scattering of the proton in matter; MCS was identified to be the main reason for the worse spatial resolution

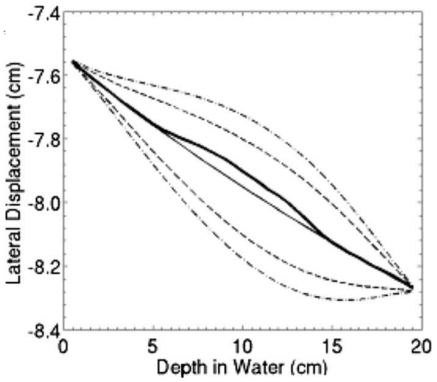

Fig. 11: Example of a reconstructed proton track using the MLP formalism; actual Monte Carlo simulated proton track (bold) and MLP output (solid line) with 2σ and 3σ limits (dashed lines) [40].

for pCT with respect to X-ray CT [50, 51], however, it is foreseen that the expected progress in MLP reconstruction algorithms can lead, in a near future, to a sensible improvement in pCT spatial resolution [40].
A major limitation is given by the slow experimental acquisition rate of the current pCT prototypes. With the best present setup, which reaches a 2 MHz acquisition rate, a complete record of the 10^9 required proton tracks-energy information would take about 10 minutes to be completed. With such long scanning times, the image quality becomes affected by motion of internal organs, mainly due to the patient's breathing. Shorter scanning times, in the order of 10 s or less, would allow the patient to hold his breath for the duration of the procedure, a measure already applied in hold-breath X-ray CT [52].
Lastly, the pCT procedure would be applied in conjunction with hadron-therapy, whose diffusion is limited by the high cost of the construction and operation of these facilities, including accelerators, beam lines, and patient delivery systems (gantries) and their maintenance. The number of patients treated with protons or heavier ions is still a small fraction of the total number of tumor-affected patients, with the X-ray therapy being the most common procedure, despite the fast growth of the number of protons and ions therapy centers, shown in Fig. 4. The cost of a proton treatment, in fact, was calculated to be roughly twice than the cost of a photon treatment [53].
Hopefully scientific and technology progress would lead, in a near future, to an improvement to the cost-competitiveness of the proton and ion therapy, as well as an advancement of the proton tomography technology. The development of low-cost compact accelerators has recently shown promising results [54].

Group	Country	Years	Tracking System	Area [cm^2]	Calorimeter	DAQ rate
UCSC - LLU NIU [43]	USA	2003-2007	2 planes x-y SSDs	6.4×6.4	CsI(Tl)	10 kHz
UCSC - LLU NIU [44]	USA	2007-2010	4 planes x-y SSDs	9×18	CsI(Tl)	20 kHz
UCSC - LLU [41]	USA	2010-2013	2 planes x-y SSDs	9×36	Plastic scintillator	2 MHz
NIU FNAL [45]	USA	2011-2014	4 planes Sci-Fi	20×24	Plastic scintillator	2 MHz
PRIMA [46]	Italy	2007-2014	4 planes x-y SSDs	5×5	YAG:Ge calorimeter	10 kHz
PREDATE INFN [47]	Italy	2013-2014	4 planes Sci-Fi	20×20	Sci-Fi	1 MHz
PRaVDA [39]	UK	2013-2015	x-y-z SSDs	9.3×9.6	CMOS APS	1 MHz
Niigata University [48]	Japan	2013-2014	4 planes x-y SSDss	9×9	NaI(Tl)	30 Hz
Tokyo-Hiroshima University [49]	Japan	2014-2016	CMOS pixels	10×10	Plastic scintillator	-
iMPACT	Italy	2016-ongoing	4 planes Si pixels	30×30	Plastic scintillator	100-500 MHz

Table 1: List of the existing pCT scanner projects and their features (updated on 2016 [30]).

3 The iMPACT Project

The *innovative Medical Proton Achromatic Calorimeter and Tracker* (iMPACT) is an European Research Council (ERC) Consolidator Grant funded project [55], hosted by University of Padova and supported by INFN, which aims to develop a high resolution and extremely fast proton computed tomography scanner apparatus. The target of the project is to reach the clinically viable acquisition rate limit, with the recording of 10^9 proton events in about 10 s, obtaining at the same time a range resolution as close as possible to the $\sim 1\%$ theoretical limit, and a competitive solution in terms of material, instrumentation and running costs. In order to meet such ambitious requirements, iMPACT plans to exploit technologies developed and currently in use for particle physics detectors. The range resolution achievable by the iMPACT scanner will be treated in Sec. 3.4.
The iMPACT scanner layout, shown in Fig. 12, consists in 4 silicon pixel sensors tracking planes, and a highly segmented plastic scintillator calorimeter, designed to be operated as a range calorimeter, measuring not the total energy but the stopping position of protons, as explained in Sec. 3.3 and 3.4. The tracking planes, grouped in two stations of two layers each, allow for the measurement of the proton trajectories entering and exiting from the patient. The use of two front and two rear tracking planes allows to estimate both position and direction of the entering and exiting proton.

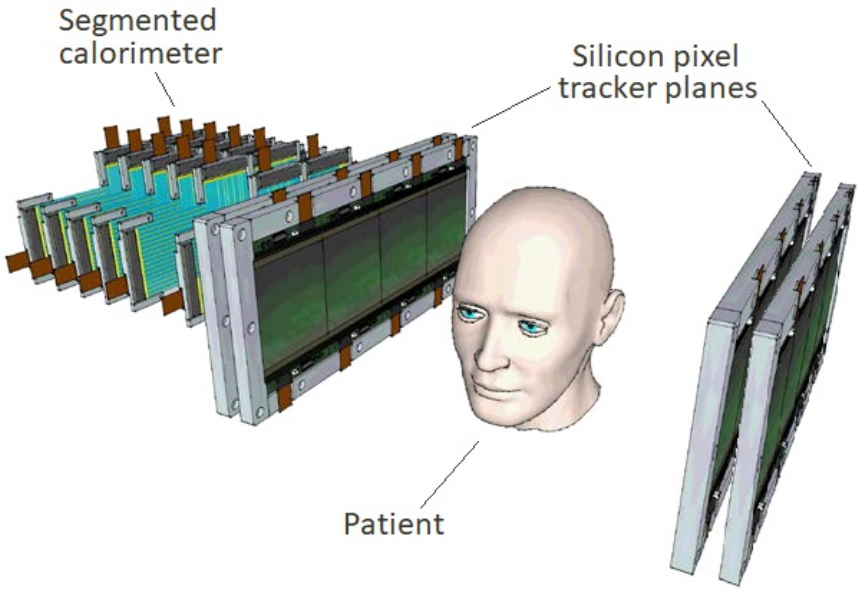

Fig. 12: Rendering of the iMPACT project scanner layout.

The iMPACT project started in 2016 with an ERC funding (Consolidator Grant 649031) of about 1.8 million euro, aiming to realize a highly innovative proton Computed Tomography (pCT) scanner prototype. The stated goal of such prototype is demonstrating that the pCT technique can be actually used in real clinical applications, even from an economical point of view.
Five staff from University of Padova form the core team of the project, while the INFN personnel actively participate in hardware development tasks. The INFN is also responsible for the purchase and commissioning of the silicon detector composing the tracker, one of the two key components of the iMPACT scanner, which will account for a relevant part of the budget. The second component, the calorimeter, is instead completely developed in-house in collaboration between Padova University and INFN.

The iMPACT team is joined by students and other collaborators from within the University, as well as by external experts which actively helps and support the development. In particular, a fruitful collaboration with the ALICE experiment strongly contributed to feasibility of the project, which will in fact exploit the INFN-backed R&D on Monolithic Active Pixel Sensors the ALICE collaboration promoted for the upgrade of its Inner Tracking System.
The iMPACT project is foreseen to last about 4 years, up to 2020, plus a possible extra year to complete the prototype characterization and/or data analysis. Further funding to the project has been granted during 2017 by the FARE program promoted by the Italian Ministry for Instruction, University and Research (MIUR).
The iMPACT project scanner is currently in its qualification and prototyping phase. The performance of both the tracker and the calorimeter are being studied separately, in order to identify the best design choices before combining them into a single instrument that correlates the information of these two separate units. The near future plan is to assemble an operating section of the setup, to evaluate the scanner performance on a reduced scale.

3.1 The tracking system

Nearly every existent pCT scanner prototype employs silicon strip detectors or scintillating fibers for tracking purposes (Tab. 1). SSDs and SCi-Fi are one-dimensional detectors, aligned to form a two-dimensional plane; two consecutive orthogonally rotated planes are necessary to measure the coordinates of the proton trajectory intersecting the detector layer. SSD and Sci-Fi-based trackers require no more than one particle passing through a tracking layer in each acquisition frame, in order to avoid possible ambiguities in the assignment of the coordinates to each proton track due to the projective readout. The maximum proton rate is therefore limited by this requirement, which turns out to be the most critical experimental issue to overcome in order to build a clinically viable pCT scanner.
The acquisition rate can be increased using a silicon pixel sensor, which can record a higher particle rate without generating any ambiguity between multiple particles, as all the relevant coordinates are measured at once by a single device. The same feature of pixel sensor allows for a substantial reduction of the material thickness that protons travel through, therefore providing the same information as SSD trackers while less affecting proton trajectory with multiple Coulomb scattering.
Several pixel sensor designs are being explored for the iMPACT project tracker. The ALPIDE sensor, developed within the ALICE Collaboration at the CERN Large Hadron Collider for the Inner Tracking System upgrade, is currently adopted in the prototyping phase while more advanced designs are still under development.

3.2 The ALPIDE sensor

The CERN Large Hadron Collider (LHC) [56], operating in Geneva (Switzerland) is planned to be upgraded by 2025, featuring a substantial increase to its luminosity and interaction rate [57]. All the experiments hosted at the LHC will be upgraded as well, in order to sustain the higher interaction rate provided.
The ALICE community designed and developed different pixel sensors for the upgrade of the Inner Tracking System (ITS). All the sensors were required to feature a high read-out rate, a spatial resolution high enough to distinguish secondary vertices, as well as low power consumption and low weight. Among the candidate sensors presented, the ALPIDE was the designated choice [58].
The ALPIDE sensor, shown in Fig. 13, is a 100 µm thick 1.5 cm × 3 cm large Monolithic Active Pixel Sensor (MAPS) featuring 28 µm× 28 µm pixels arranged in a 512 × 1024 matrix [58]. Each pixel output is binary, being it 1 when enough charge from the ionization due to a charged particle hitting the detector is collected by the pixel diode. The chip is produced with the TowerJazz

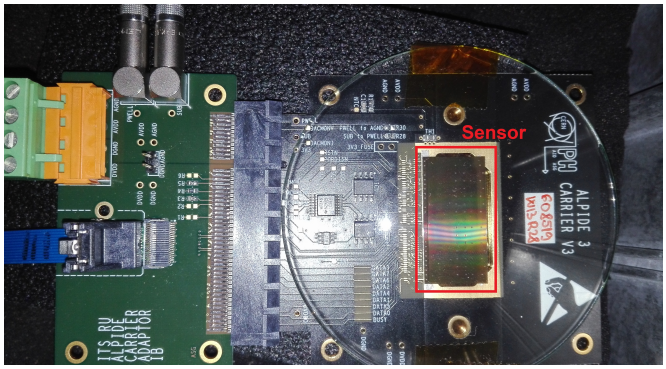

Fig. 13: The ALPIDE sensor (highlighted in red), mounted on a carrier board and connected to the read-out cable adapter board.

180 nm CMOS Imaging Process [59]. This technology provides a high level of integration, allowing the CMOS-based read-out electronics to be implanted directly over the pixel sensitive epitaxial layer, where the particle charge deposition takes place (monolithic design), as shown in Fig.14. The in-pixel electronics includes a continuously active discriminating amplifier, with a 2 µs shaping time, which identifies hit pixels, and an multiple event memory. The read-out electronics implements a zero-suppression logic, which means that only hit pixels are read out. The sensor is able to cope with a 100 kHz/cm^2 particle rate, most limited by the read-out bandwidth of 1.2 Gbit/s. The charge collection in the ALPIDE sensor can be enhanced by applying a reverse bias to the substrate [60].

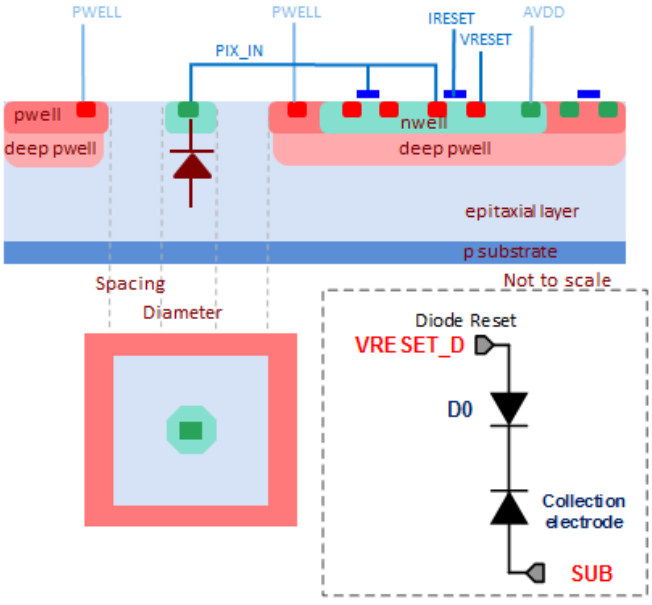

Fig. 14: Schematic view of the monolithic design used for ALPIDE pixels; the particle charge deposition takes place in the epitaxial layer, the CMOS read-out electronics directly implanted on the pixel [61].

Tests with different particles (e^- and π) and different energies (from 60 MeV to 120 GeV) were conducted on several ALPIDE sensors. The detection efficiencies were found to be above 99.6% in all considered sensors, while the fake hit rates were significantly below 10^{-6}/event

per pixel [58]. ALPIDE reaches a sub-pixel spatial resolution around 4.6 µm: because of charge diffusion, each charged particle fires a cluster of adjacent pixels, whose typical size is 3-4, allowing for a better resolution on the hit position measurement than the typical one given by pitch/$\sqrt{12} \approx 8$ µm resolution.
Furthermore, the ALPIDE monolithic design allows the sensor to meet the low assembly, production and material cost [58] requirements, as well as a low power consumption (< 50 mW cm^{-2}), in fact, the integration of the front-end stage and the collection node, enabled by the monolithic approach, makes it possible to minimize the parasitic capacitance down to the fF level, therefore maximizing the Q/C ratio and lowering the bias current of the first stage.

3.3 The energy-range calorimeter

The iMPACT scanner includes, together with the tracker system, a highly segmented scintillator calorimeter. The iMPACT calorimeter is designed to serve as a range detector, estimating the proton stopping position, instead of directly measuring its residual energy, like in traditional setups.
The planned iMPACT calorimeter, outlined in Fig. 15, is segmented in the z direction into 5 mm thick plastic scintillator planes with about 40×40 cm^2 surface area; a total of around 60 planes is foreseen, to completely stop a $\sim$ 200 MeV proton beam. Each plane is further divided into smaller segments, also referred to as *fingers*, each one 1 cm wide and 20 cm long. Consecutive planes, also referred to as x or y planes, alternate fingers aligned along the x and y directions. Each scintillating finger is independently read-out with a Silicon Photo Multiplier (SiPM). SiPM technology will be dealt in detail in Sec. 3.5. Each finger is wrapped with a thin, highly reflective teflon layer, to improve light collection.

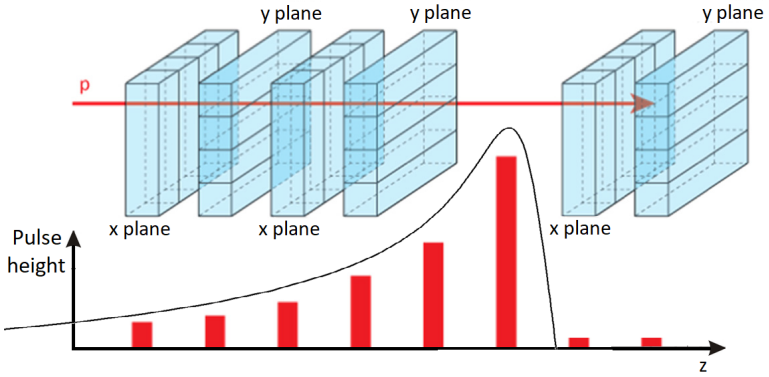

Fig. 15: iMPACT calorimeter layout, segmented in alternate x and y planes. Red bars represent the expected signal amplitudes along the planes.

The iMPACT calorimeter can provide proton range measurements with three progressively more accurate modalities, according to the needed precision. In the first approximation the energy deposited by a proton is integrated over an entire plane. The energy information is then used in a binary hit-miss fashion: the detection of a signal exceeding a fixed threshold indicates the passage of a proton in a given plane. The projection of the proton range along the z axis can therefore be assumed to be the mean point of the last hit plane, with an uncertainty given by the z-direction segmentation pitch (5 mm) divided by $\sqrt{12}$.
This coarse estimate can be refined considering each finger individually, exploiting the x-y segmentation of the calorimeter. The proton range can be calculated as the sum of the segments connecting the midpoint of hit fingers. In this case the trajectory of the proton along its path inside the calorimeter can be followed, taking into account the lateral deviation of the proton, and leading to a measurement of not just the range z-projection but the actual proton path

length.
The most accurate estimate can be obtained taking into consideration the values of the energy deposited in each finger. The output signal heights can be used to reconstruct the shape of the proton Bragg curve, which can then be fitted in order to calculate the proton stopping position, as shown in Fig. 15. In this case the proton range can be obtained with a sub z-pitch precision. Uncertainty on the proton range estimation are extensively dealt with in Sec. 3.4.
Furthermore, the high level of segmentation in the x-y plane allows a higher detection rate capability of the scanner. In fact, having a greater number of fingers reduces the probability of more than one proton passing through the same finger during an acquisition window.
Polyvinyltoluene (PVT) scintillators, manufactured by Saint-Gobain, have been chosen, due to their fast time response, with less than a ns raising time, good light yield, more than 11000 photons/MeV [62, 63]. Furthermore the low density of approximately 1 g/cm^3, makes PVT less demanding for the support elements. Two different products are being taken into consideration: the BC-420, slightly faster, and the BC-408, with emission wavelengths better matched by the SiPM efficiency. BC-420 and BC-408 scintillator properties are presented in Tab. 2, while the light output wavelength distributions are shown in Fig. 25.

	BC-420	**BC-408**
Densitiy [g/cm^3] , [% Anthracene]	1.032 , 64%	
Refractive index	1.58	
Light yield [photons/MeV]	11136	
Max emission wavelenght [nm]	391	425
Raise time [ns]	0.5	0.9
Deacay time [ns]	1.5	2.1
Light attenuation lenght [cm]	140	210

Table 2: BC-420 and BC-408 polyvinyl toluene declared parameters. Data retrieved from Saint-Gobain data sheet [62, 63].

The iMPACT calorimeter is designed to have a completely modular layout. In the current project state, the basic unit, shown in Fig. 16, consist in 48 fingers arranged parallelly in 4 planes. A single module holds scintillating fingers, SiPM, read-out electronics and input-output ports, while being mechanically self-sustaining. An x-y sector can be set up combining two orthogonally rotated modules, as shown in Fig. 17. Lastly, a full surface layer can be obtained with 4 x-y sectors. The entire calorimeter can be therefore assembled using identical modules repeatedly, contributing to keep costs down.

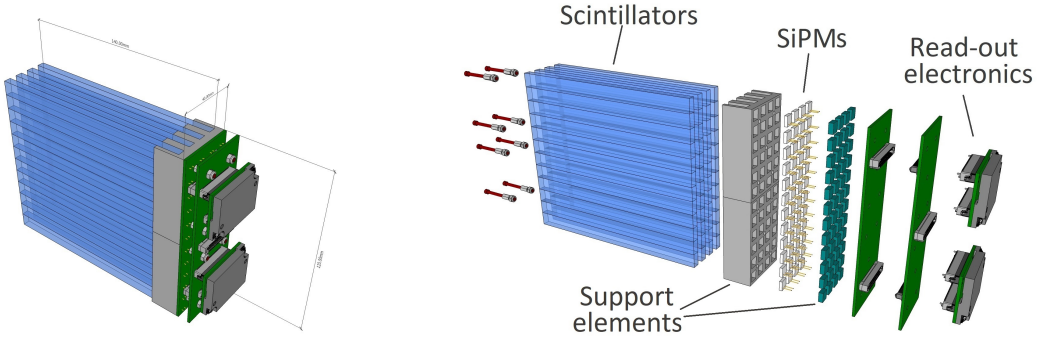

Fig. 16: 3D rendering of a iMPACT calorimeter single module, assembled (left) and exploded view (right).

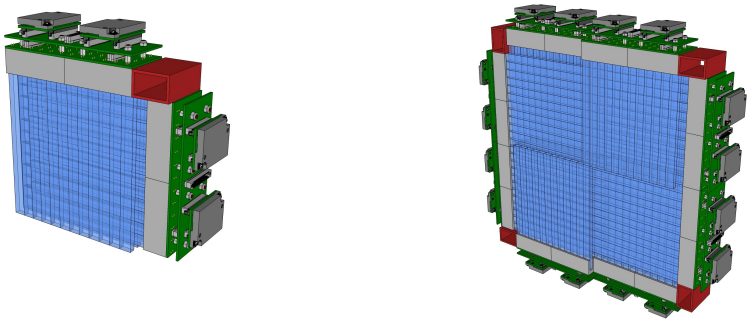

Fig. 17: iMPACT calorimeter modular layout; a combination of 2 single modules forms a x-y sector (left); 4 x-y sectors are combined to form a complete layer (right).

Considering the complete calorimeter (for example 60 planes with 48 fingers each, for a total of >2800 fingers) the number of SiPM output channels would be extremely high. Having more than 1000 analog channels sampled at GHz frequency, yet possible, would be quite impractical, power consuming and expensive, missing the project goal of a functional and economically viable medical pCT. After considering many options, a threshold-based digital discriminator was chosen; this concept is presented in Fig. 18. The analog SiPM output signal is sampled at a number of different amplitude levels (less than 5) by fast comparators, which provide the information of the level reached by the signal and the time a certain level is exceeded. The data is then sent to an FPGA for sparsification (channels below a minimum threshold are discarded), formatting and delivery for the following analysis. This system is comparable to a 2 or 3 bit ADC. The number and the level of the thresholds are to be optimized from both simulations and experimental data; for this reason, in the early prototyping phase of the project, while the number of channels is still manageable, the output signals are digitized with full precision, resulting in highly-detailed waveforms.

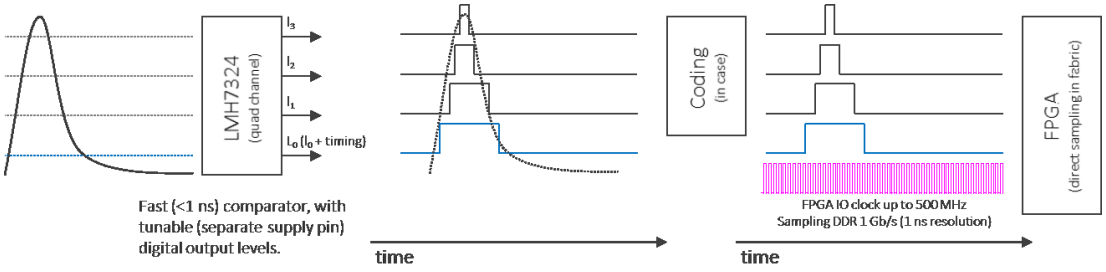

Fig. 18: Concept of threshold-based digital discriminator with 4 threshold levels sampled by fast comparators.

3.4 Range resolution in proton tomography

Water equivalent path lenght (WEPL) can be expressed as the integral along the proton path L inside the absorber material of the relative stopping power RSP, defined in Eq. 15:

$$\text{WEPL} = \int_L \text{RSP}(l)dl \tag{16}$$

where RSP(l) is the relative stopping power at l distance along the path.
A general pCT energy detector calorimeter is formed by a number n of consecutive scintillator layers, aligned in the direction of the beam z, with each scintillator layer having a water equivalent thickness Δz, as shown in Fig. 19. The total calorimeter thickness $n\Delta z$ has to be enough to stop all the protons.

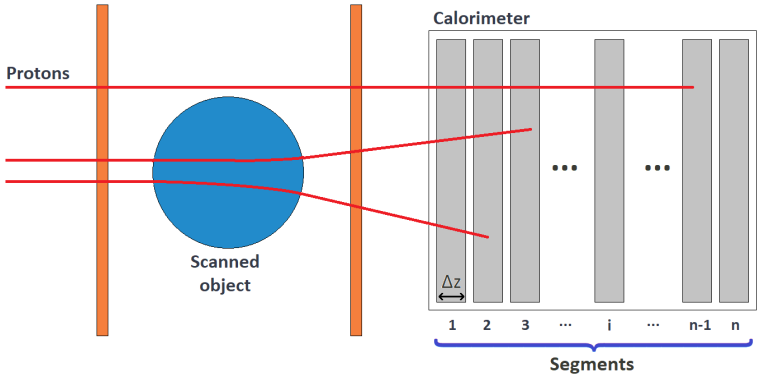

Fig. 19: Schematic view of a pCT scanner with segmented calorimeter.

The WEPL inside the scanned object of a monoenergetic proton beam with a total range in water R_{tot}, as defined in Eq. (7), can be estimated by:

$$\text{WEPL} = R_{\text{tot}} - R \tag{17}$$

where R is the water equivalent distance travelled by the protons in the calorimeter volume.
In case of a single-volume calorimeter, i.e. $n = 1$, the protons residual energy is measured, and its range has to be inferred with the Bragg-Kleeman rule (8). This estimate of WEPL is affected by two uncertainty sources: the intrinsic range straggling σ_R^{stragg}, which is around 1.1% of the range value, so $\sigma_R^{\text{stragg}} \approx 0.011 \times (\text{WEPL})$, and the experimental uncertainty derived from the Bragg-Kleeman rule $\sigma_R^{\text{exp}} \approx pR \cdot \delta E$, where δE is the energy resolution of the calorimeter. Assuming the two uncertainty sources to be uncorrelated, the total uncertainty on a measure of WEPL, σ_{WEPL} is the quadratic sum of the two terms:

$$\sigma_{\text{WEPL}} \approx \sqrt{[0.011 \times \text{WEPL}]^2 + [p(R_{\text{tot}} - \text{WEPL})\delta E]^2}. \tag{18}$$

Eq. (18) is an approximate expression, because the straggling on the range inside the calorimeter is not considered. In order to reach the theoretical limit of $\sigma_{\text{WEPL}} \sim \sigma_R^{\text{stragg}}$, the experimental term has to be small with respect to the straggling term, for a sufficient range of WEPL values; to meet this requirement, the energy resolution of the calorimeter has to be better than 1% for a large range of energies, representing a real challenge for the construction of a calorimeter which needs to be fast as well [64].
An alternate WEPL measurement concept consists in a range counter: the calorimeter is composed by a large number of layers ($n \gg 10$) and the range R of a proton is deduced by the number of calorimeter layers i that registered a signal. The WEPL estimation from Eq. (17) becomes:

$$\text{WEPL} \approx R_{\text{tot}} - (i-1)\Delta z - \frac{\Delta z}{2} \tag{19}$$

considering the center position of the last hit segment as the stopping point. In this case the straggling term of σ_{WEPL} is calculated as 1.1% of the total range R_{tot}, while the experimental uncentainty is given by $\Delta z/\sqrt{12}$, assuming a uniform probability inside the i-th segment. The

total WEPL uncertainty is indipendent WEPL and can be expressed as:

$$\sigma_{\mathrm{WEPL}} \approx \sqrt{(0.011 \times R_{\mathrm{tot}})^2 + \left(\frac{\Delta z}{\sqrt{12}}\right)^2}. \tag{20}$$

The requirement of the experimental contribution to σ_{WEPL} being negligible, according to (20), is then substantially met if $\Delta z < 0.015 \times R_{\mathrm{tot}}$, which is approximately 4 mm for 200 MeV protons [64].
Another solution, developed at Loma Linda University (LLU, California) consists in a calorimeter with a small number of layers, e.g. n=5 [44]. This calorimeter design serves both as a range counter and energy measurement device, providing both the identification of the i-th layer where the proton comes at rest and the energy E_i collected therein. The proton path length in the calorimeter is then calculated as the thickness on the first $(i-1)$ layers plus the path in the i-th one, calculated with the Bragg-Kleeman rule (8), resulting in the following modifications of Equations (19) and (20), respectively:

$$\mathrm{WEPL} \approx R_{\mathrm{tot}} - (i-1)\Delta z - \alpha E_i^p \tag{21}$$

$$\sigma_{\mathrm{WEPL}} \approx \sqrt{[0.011 \times (R_{\mathrm{tot}} - \alpha E_i^p)]^2 + (p \cdot \alpha E_i^p \cdot \delta E)^2}. \tag{22}$$

The WEPL resolution σ_{WEPL} as a function of WEPL is presented in Fig. 20(a), for the different approaches; 200 MeV protons are considered, with an equivalent total range in water $R_{\mathrm{tot}} \approx 25.6$ cm and a straggling ${\sigma_R}^{\mathrm{stragg}} \approx 2.8$ mm. The parameter p in (8), which appears in (18) and (22) as well, was estimated to be around 1.7 for the plastic polystyrene-based scintillator, used in [44], from a fit of NIST energy-range data [65](Fig. 74 in Appendix). Fig. 20(a) shows that the hybrid energy-range calorimeter solution outperforms both the a single-layer calorimeter and the simple range counter with $n = 60$ segments, in a wide range of WEPL values. In Fig. 20(b) the measured and simulated WEPL resolutions in the configuration $n = 5$ and $\delta E = 2\%$ are shown [64]. In this configuration measured resolutions span between 2.8 mm, corresponding to the $0.011 \times R_{\mathrm{tot}}$ straggling limit, and 3.5 mm.

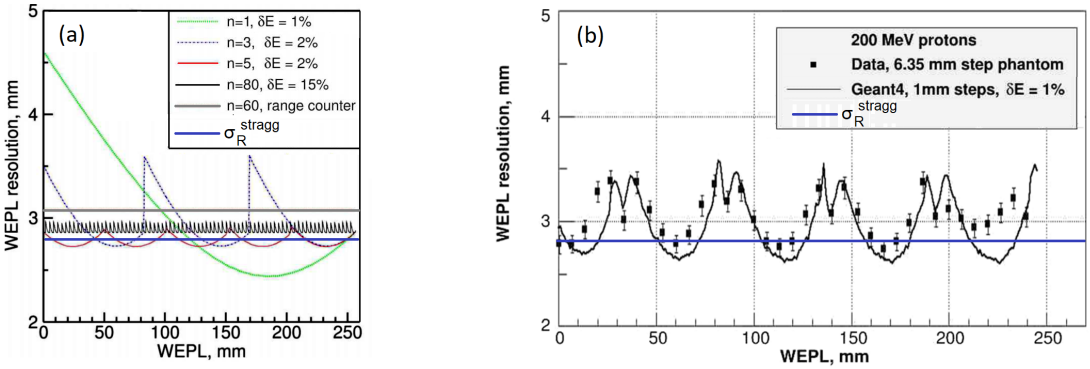

Fig. 20: (a) Predicted WEPL resolutions σ_R as a function of WEPL for different calorimeter designs; (b) Measured and simulated σ_R in the configuration $n = 5$, $\delta E = 2\%$. $E = 200$ MeV, $R_{\mathrm{tot}} \approx 256$ mm and $\sigma_R^{\mathrm{stragg}} \approx 2.8$ mm (blue solid line), adapted from [64].

The iMPACT calorimeter was designed to serve as an improved version of a range counter, with $n \approx 60$ and $\Delta z = 5$ mm, providing both range and energy information. As can be seen in Fig. 21, the knowledge of the $i-$th layer where the proton comes at rest limits the proton range in the interval $[(i-1)\Delta z\ ;\ i\Delta z]$, while the energy deposited in the layers can be used for an improved estimate of the proton stopping position inside the i-th layer.

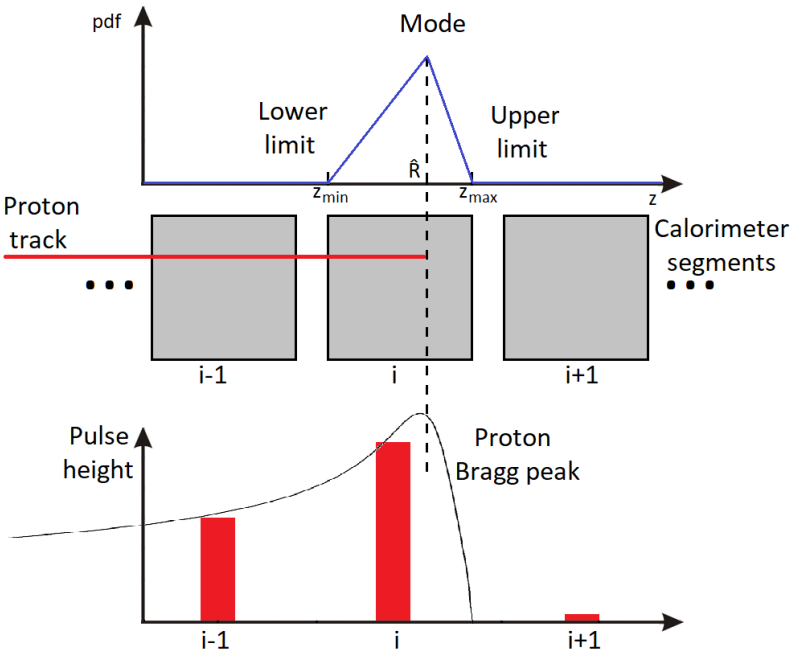

Fig. 21: Concept of an hybrid calorimeter, exploiting both range and energy information. The pdf describing the knowledge of the proton stopping position, based on energy deposition in the calorimeter layers, is the triangular distribution.

The probability density function (pdf) of a variable with known lower and upper limit, $z_{\min}$ and $z_{\max}$ respectively, and an educated guess on the most likely value $\hat{R}$ (mode) is the triangular distribution, also known as the *lack of knowledge* distribution [66]. The variance of a triangular distribution is given by:

$$\left(\sigma_R^{\text{triang}}\right)^2 = \frac{{z_{\min}}^2 + {z_{\max}}^2 + \hat{R}^2 - z_{\min} z_{\max} - z_{\max}\hat{R} - z_{\min}\hat{R}}{18}. \tag{23}$$

The WEPL and its resolution can be therefore estimated according to this procedure by modifying Eq. 21 and 22 as:

$$\text{WEPL} \approx R_{\text{tot}} - (i-1)\Delta z - \hat{R} \tag{24}$$

$$\sigma_{\text{WEPL}} \approx \sqrt{[0.011 \times (R_{\text{tot}} - \hat{R})]^2 + (\sigma_R^{\text{triang}})^2}. \tag{25}$$

Fig. 22 shows the different contributions to σ_{WEPL} predicted for the iMPACT calorimeter. The experimental uncertainty σ_R^{triang} (red line) oscillates between 1 and 1.5 mm, almost 1/3 of the intrinsic straggling term $\sigma_R^{\text{stragg}} = 0.011 \times (R_{\text{tot}} - \hat{R})$ which is about 2.8 mm (blue line), so the total WEPL uncertainty σ_{WEPL} (green line) is dominated by the latter. The total WEPL resolution is expected to span between 3 and 3.2 mm, close to the theoretical limit of 2.8 mm given by the intrinsic variance of the physic process, so further improvements on the experimental resolution would not lead to a substantial improvement of the total WEPL resolution. The expected WEPL resolution is comparable to the resolution obtained in the configuration with $n = 5$ and $\delta E = 2\%$, presented in Fig. 20. It is also worth to recall that σ_R^{triang} is also smaller than the resolution of the iMPACT calorimeter when used as a simple range counter, i.e. neglecting the energy information, in which case $\sigma_R^{\text{counter}} = 5 \text{ mm}/\sqrt{12}$.

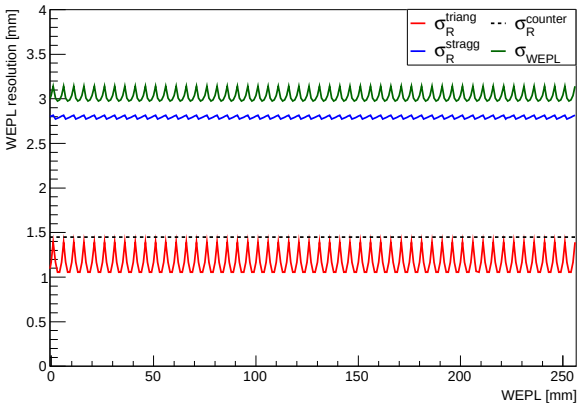

Fig. 22: Foreseen WEPL resolution of the iMPACT calorimeter as a function of WEPL (green line). The experimental term from Eq. (23) σ_R^{triang} (red line) and the intrinsic uncertainty due to straggling (blue line) are shown as separate contributions. The expected experimental resolution when the iMPACT calorimeter is operated purely as a range calorimeter is shown as well (black dashed line).

3.5 SiPM (MPPC) technology

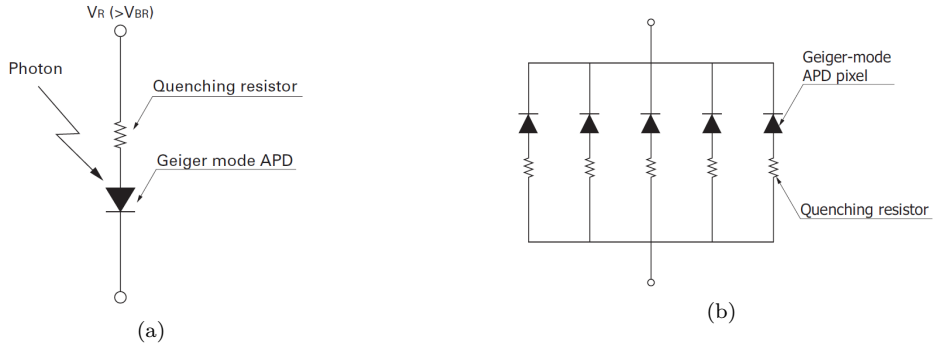

Fig. 23: (a) Geiger mode APD and quenching resistor. V_R: Reverse voltage, V_{BR}: Breakdown voltage. (b) The configuration in parallel of multiple APD to form a SiPM.

Each scintillating finger is coupled with a Silicon Photo-Multiplier, which converts the optical scintillation photons into an analog signal. A Silicon Photo-Multiplier (SiPM), also referred to as Multi Pixel Photon counter (MPPC), is a solid state photon-counting device, developed for low light level detection, and intended to be an alternative to photomultiplier tubes (PMT). These devices provide high photon detection efficiency, up to 40%, active area smaller than cm, low operating voltage ($\sim$ 60 V), below-ns timing response, good time resolution, up to 250 ps, wide spectral response range and are unaffected by magnetic fields [67].
The SiPM is made up of multiple independent Avalanche PhotoDiodes (APD) operating in Geiger mode: a reverse voltage, higher than the breakdown voltage, is applied to each APD, so that even the charge induced by a single photon can result in a Geiger avalanche discharge. In this condition the electron gain is $10^5 - 10^6$, so the output current of each APD is constant and independent from the number of incident photons. The APD is blind to photons incoming during the discharge process, and a quenching resistor is included in series with the APD in order to stop the discharge: the current flowing through such resistor reduces the voltage on the APD, hence stopping the avalanche. The time that is necessary to the APD to be capable

of detecting new photons after a photon hit is called quenching time t_{quench}, which ranges between 20 ns and 150 ns in different commercial SiPM products. A typical output signal of a single APD cell is shown in Fig. 24 [68]: the voltage reaches its maximum in ~ 0.5 ns after the arrival of a photon, decaying exponentially afterwards. The fast signal rise makes SiPM devices particularly suitable for applications requiring good timing resolutions.
A number of APD and quenching resistors are connected in parallel to form the bidimensional array of pixels of a SiPM. The resulting signal features the same amplitude for each pixel in the SiPM, and signals from each pixels are summed to each other, as in Fig. 23(b), so that the detection of multiple photons results in a signal which is proportional to the number of pixels hit. The relation between the signal amplitude and the number of detected photons is linear as long as the number of simultaneous photons is low enough to have a negligible probability for two or more photons to hit the same APD pixel.
SiPM photon detection efficiency can be calculated as the product of quantum efficiency, fill factor and avalanche probability. Quantum efficiency is defined as the probability for an incident photon to release charge carries, fill factor takes into account the ratio between the active and the total area, and avalanche probability is the probability for the freed charges to undergo multiplication, which is affected by the bias voltage applied to the device. SiPM detection efficiency peaks between 400 nm and 500 nm.
Hamamatsu SiPM have been chosen for the iMPACT prototype development, due to their competitive technical features and the fact that they are offered in a ceramic mounting package that greatly helps system integration, a key benefit considering the great number of SiPM foreseen for the final calorimeter. Hamamatsu SiPM are produced with different APD cell size, between 10 µm and 100 µm pitch. SiPM with smaller pixel pitch are more suitable for applications in which high photon fluxes are expected, while larger pixels guarantee a higher geometrical fill-factor, and a overall higher detection efficiency. Hamamatsu S12572-025c, with 25 µm pixel pitch, have been chosen, which represent a good compromise between efficiency and photon detection rate. The photon detection efficiency as a function of wavelength for the chosen SiPM model is shown in Fig. 25; in the same plot the light output distribution of the two PVT scintillator considered (Saint-Gobain BC-420 and BC-408) is also presented. The SiPM efficiency matches both light output distributions, however the BC-408 emission is closer to the SiPM efficiency maximum.

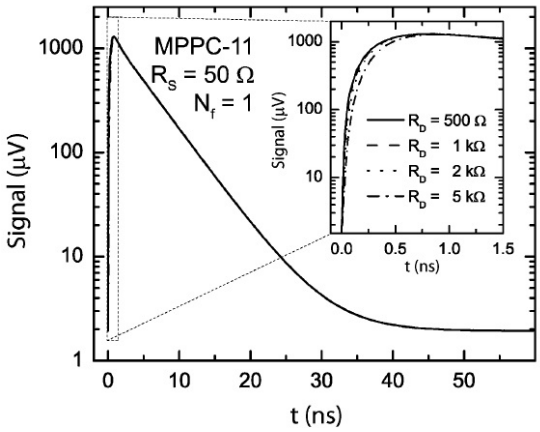

Fig. 24: Simulated signal of a single cell of a HAMAMATSU S10362-11-25u SiPM with 25 µm pixel pitch [68].

The quenching time for the chosen SiPM model is not yet known, as extensive characterizing studies have not yet been carried out by neither iMPACT group nor other groups. An estimate of the quenching time can be obtained using a pulsed light source with a known intensity. The

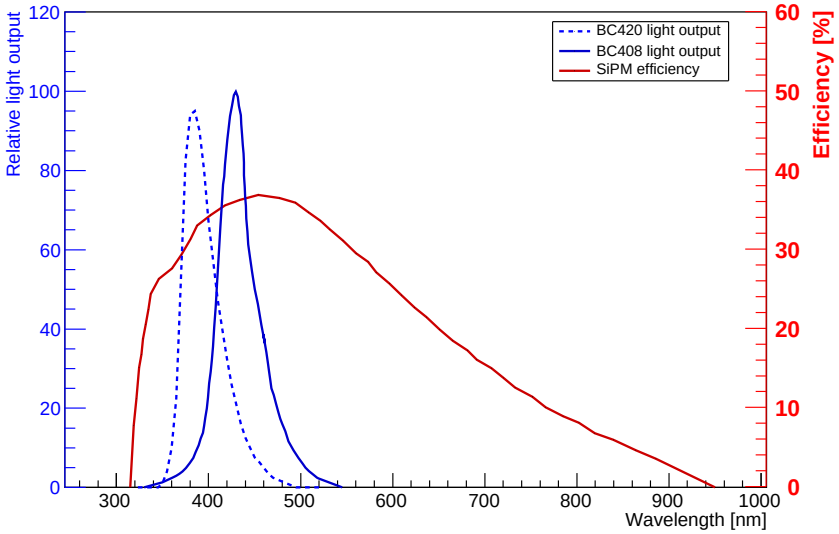

Fig. 25: Scintillators (BC420 and BC408) light output as a function of the wavelength (primary axis) compared to SiPM detection efficiency (secondary axis). Data retrieved from Hamamatsu and Saint-Gobain data sheet [62, 63, 67].

amplitude of the SiPM output signal is observed at varying light impulses delay, as shown in Fig. 26 for a Hamamatsu 3 mm×3 mm prototype; at delays longer than the quenching time the output signal is saturated, as the hit APD cells can recover between two consecutive pulses, while at lower delays the signal decreases [69]. A quenching time test for the SiPM chosen for the iMPACT calorimeter is planned in the near future.

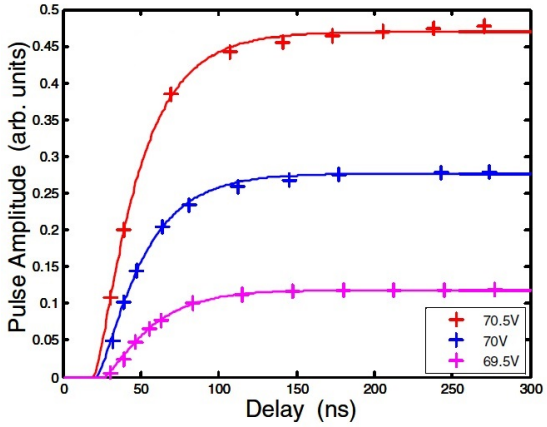

Fig. 26: Hamamatsu 3 mm ×3 mm SiPM prototype pulse amplitude as a function of light impulses delay, for different bias voltage, to estimate the quenching time [69].

4 Simulations of the basic unit of the iMPACT calorimeter

A Monte Carlo simulation of the calorimeter has been developed in order to evaluate its performance. The simulation is used, in a first phase, to optimize the detector constructive parameters, while, in a more advanced stage, the simulation will provide experimental-like output data for testing the read-out chain, the data analysis software, and the image reconstruction techniques.
The simulation was modelled using the GATE application, an advanced opensource software dedicated to numerical simulations in medical imaging and radiotherapy [70], based on the Geant4 toolkit [71]. The interface provided by GATE to the Geant4 libraries allows to define volumes, materials and their physical properties to each volume, including density, atomic number and optical properties. Different kind of particle sources can be defined, from pencil-beams to emitting volumes, with customizable energy spectra and particle rate. Moreover particle detectors can be implemented, with parameterized response and read-out chain.
The simulation studies discussed in the following Sections have been focused on the characterization and modelling of the scintillation process and the detection of photons in a single PVT finger, which represents the basic unit of the iMPACT calorimeter. Further simulation studies, including more complex multiple fingers setups, will be discussed later, together with the comparison with experimental data.
The full transport of optical photons is employed at this early characterization stage, while future developments of the iMPACT calorimeter simulation will employ parameterizations of the measured output signal, once the fundamental technical choices of both scintillator material and read-out electronics will be consolidated after the currently ongoing evaluation.

4.1 Simulation of a scintillator finger

A single finger is modelled as a 1 cm $\times$ 0.5 cm $\times$ 20 cm box, with polyvinyl toluene assigned as the constituent material and a teflon wrapping. A 3 mm $\times$ 3 mm $\times$ 1 mm silicon box, representing the SiPM, is placed on top of the finger, as shown in Fig. 27. These volumes are defined inside a bigger air-filled volume (referred to as *world* in the GATE software); the world material can be changed into vacuum accordingly to the experimental setup.
The chemical properties of the materials can be defined by the user in a dedicated file: the polyvinyl toluene material was included, specifying its stoichiometric composition (C_9H_{10}), and density (1.032 g/cm^3), as as listed in Tab. 2, according to the manufacturer specifications [62, 63]. The following optical properties of PVT can be defined as well: light yield, fast and slow scintillation time constants and the relative weight of such components, refractive index, light attenuation length, light emission spectrum, and energy resolution. BC-420 is the only scintillator type that has been characterized within iMPACT, in this early prototyping stage, with enough detail for simulation purposes. The light yield has been set to its nominal value of of 11136 photons/MeV, as well as the fast time constant, refractive index and attenuation length. The data sheet available from Saint-Gobain do not report any slow component for their organic scintillators, therefore only the fast time constant is used, while additional characterization is needed on this particular property. An estimation of PVT parameters via experimental data is presented in Sec. 5.
The light emission spectrum is a function of the wavelength, as opposed to the previous parameters which are constant; in GATE this is referred to as a *vector property* and has to be tabulated in detail by wavelength values. The simulation studies presented herein are based on a fine-grain sampling of the emission spectrum provided by Saint-Gobain, shown in Fig. 25, which has been used to define such vectorial form of this material property.
The energy resolution of a scintillator must be expressed, according to GATE, in terms of σ_N, the error on the number N of photons emitted for a given deposited energy; the energy

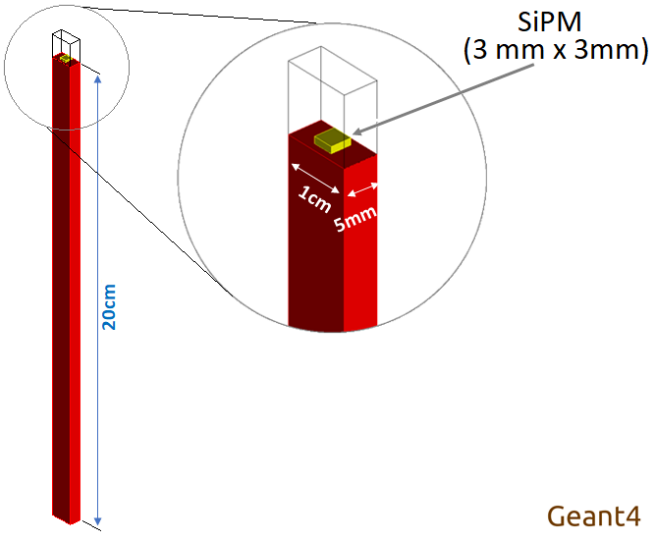

Fig. 27: Single PVT scintillating finger modelled with GATE. Particular of the 3 mm×3 mm SiPM on one of the finger bases.

resolution is than parametrized with the resolution scale value RS, defined as:

$$\sigma_N = \mathrm{RS} \times \sqrt{N} \tag{26}$$

where N is the number of emitted photons. The RS parameter has to be adjusted using experimental data.
A proton pencil-beam source is defined. The energy spectrum and position of the source can be modified accordingly to the experimental condition that has to be simulated.
Needed physics processes have to be activated by the user, choosing between different theoretical models and cross section data tables. Geant4 however offers a number of preset physics lists suited for different energy ranges and different applications. The *Low Background Experiments* (LBE) physics list was selected for this simulation, being the only one among preset lists that supports also optical processes, including scintillation, Rayleigh scattering, optical photons absorption, Mie scattering and wavelength shift. In this simulation Birk's law has not been implemented.
To validate the choice of the LBE physics list, the proton energy loss obtained from GATE has been compared with proton energy loss computed using two other simulation codes, Fluka [72] and SRIM [73]; the results are shown in Fig. 28. The proton range simulated with Geant4 loading the LBE physics list is in good agreement with Fluka and SRIM, within 0.5%, confirming the suitability of the chosen physics list for the particular purpose of studying the expected behaviour of scintillators being evaluated for iMPACT.
Fig. 29 shows an example visualization of a single proton interacting with the scintillator simulated in GATE. Optical photons, proportional in number to the amount of the energy lost by the proton, are isotropically generated along its path through the PVT.
Each scintillation photon is individually transported in the material, and the optical behaviour at volume boundaries is simulated. Different surfaces properties, as the finger teflon wrapping, have been defined, in order to simulate a realistic optical behaviour of photons. The optical properties of teflon are natively tabulated in Geant4 according to two options, *polished* and *rough* wrapping, both featuring a 95% reflectivity and 0% transmission probability. The simulation tool allows to implement the presence of micro-facets on the surface, described by the σ_α parameter, which is defined as the standard deviation of the distribution of micro-facets normal direction, around the average surface normal. The photon reflection angles are according to

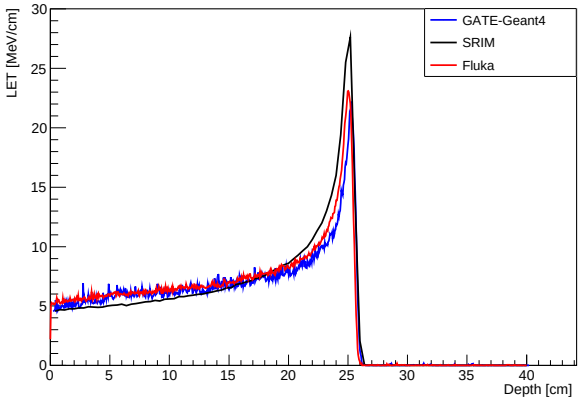

Fig. 28: Proton energy loss simulated with different codes: Geant4, SRIM and Fluka.

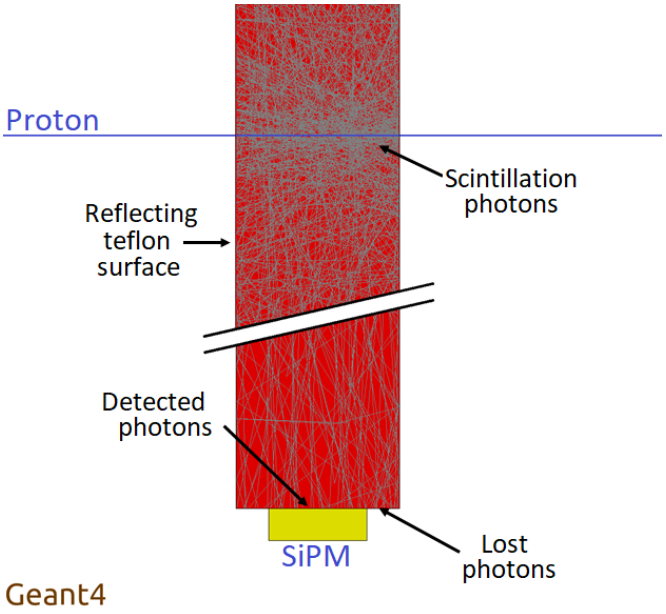

Fig. 29: Simulated scintillation process for a proton (blue), transportation of optical photons (grey) and different surface properties. The number of generated photons has purposely been reduced by a factor ~ 1000, to help visualizing single photon tracks.

Snell's Law with respect to the micro-facets surface [74]. A $\sigma_\alpha = 1$ is assigned to polish teflon, while a $\sigma_\alpha = 6.0$ is assigned to the rough teflon; in this simulation the second option has been chosen, as fingers in the early prototypes discussed herein are hand-wrapped in teflon.
A teflon wrapping has been defined for every side of each finger, with the exclusion of the one optically coupled to the SiPM. The boundary between the finger and the SiPM is defined in GATE as a *dielectric-metal* surface, the probability of photon reflection or transmission between the two materials is calculated according to the Fresnel equation. The SiPM surface in contact with the finger constitutes the primary signal detector: photons transmitted in the SiPM silicon volume are recorded. The SiPM detection efficiency as a function of wavelength is described as a vector property of the surface, using the distribution provided by Hamamatsu, shown in Fig. 25.
The remaining area of the finger, which is covered by neither teflon nor silicon, is defined as an

absorber: transmitted photons, which actually would exit the PVT without being reflected nor detected, are not further transported by Geant4. The described behaviour of photons resulting from the scintillation process is summarized in Fig. 29: the majority of photons produced by the proton are reflected by the lateral teflon surface, those reaching the PVT-SiPM interface are detected, while those leaving the PVT volume through the unwrapped fraction of the lower base are lost.

4.2 Simulation of the output signal and measurements of the single photon response

Photons detected by the SiPM, taking into account the detection efficiency, are recorded. The simulation provides for each photon, among others, the following parameters: detection time, detection position, photon energy, a code identifying the corresponding primary proton and different codes corresponding to physical processes affecting the photon during its existence. From these information the analog SiPM output signal is derived.
All SiPM produce an identical impulse each time a photon is detected, so a multiple-photon signal is given by the overlap of multiple single-photon voltage pulses. Photon collection time is obtained from the simulation, therefore the analog simulated signal can be built by summing the same single-photon response for each detected photon, with the starting time of each pulse given by the photon detection time as shown in Fig. 30. In (a) the photon detection time distribution is shown, the simulated signal presented in (b) is obtained from summing the single-photon pulse each time a photon is detected. The analog signal corresponding to a single photon can be measured and parameterized for this purpose, according to the procedure discussed herein. This signal reconstruction method assumes a negligible quenching time on the SiPM APD cells. The validity limits of this assumption are discussed in Sec. 7.

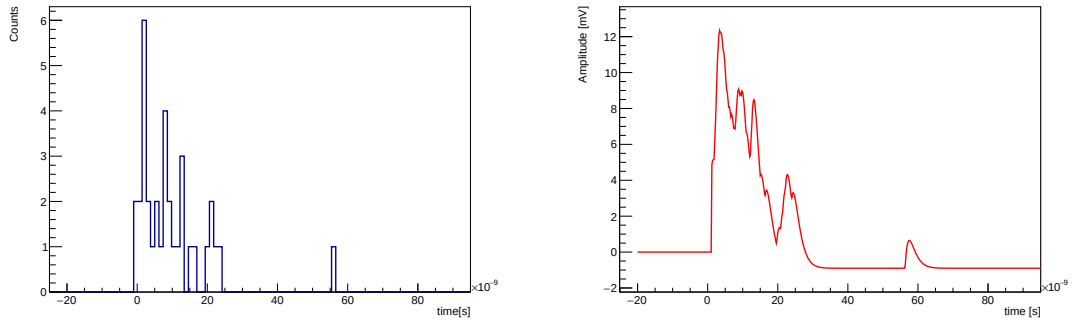

(a) (b)

Fig. 30: (a) Photon detection time spectrum, obtained from the GATE simulation. (b) Simulated signal, derived from the time spectrum.

The measured signal for a single photon is the result of the APD pulse from the SiPM, which is then shaped by the read-out electronics. The simulation outputs the reconstructed signals in the same format of the ADC, presented in Sec 5, used to digitize experimental waveforms, meaning that the very same analysis tools can be used to process both experimental and simulated data.
Direct measurements of a very low intensity light source allow to measure the signal, resulting from a single photon, after the SiPM pulse is shaped by the read-out electronics. The contribution of single photons can be derived from signals produced by a countable and low number of simultaneous photons hitting the SiPM.
The apparatus for the single photon response measurement, is shown if Fig. 31. It is built around a PicoQuant PLS-592 pulsed LED, featuring monochromatic $\lambda \approx 600$ nm light emission, sub-

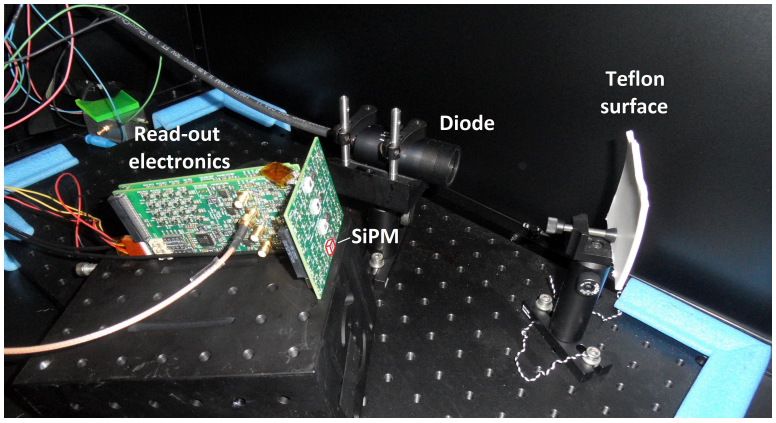

Fig. 31: Experimental setup for the single photon response measurement.

nanosecond pulse time width and adjustable intensity [75], piloted with a PicoQuant pulsed driver PDL 800-B, with selectable pulse frequencies between 2.5 and 80 MHz [76]. A teflon surface reflects and diffuses back the light beam produced by the LED, which is then detected with the full SiPM-read-out chain. The schematic of the custom read-out electronics is shown in Appendix, Fig. 38. The entire apparatus is enclosed in a sealed dark chamber, to isolate the instruments from external light sources. The analog SiPM output waveform is capture by a Tektronix DPO 7354 fast oscilloscope, with the external trigger driven by the pulse generator. A delayed coincidence with the driver pulses is used to reject dark-count signals and room background, as the distance travelled by photons from the emitting diode to the SiPM results in a constant, known delay, around 2 ns.
The emitting diode is driven such that to minimize the emission intensity, and the number of photons detected by the SiPM is approximately 10. Fig. 32 shows a screen-capture of the oscilloscope, featuring several overlying waveforms corresponding to different numbers of simultaneously detected photons.

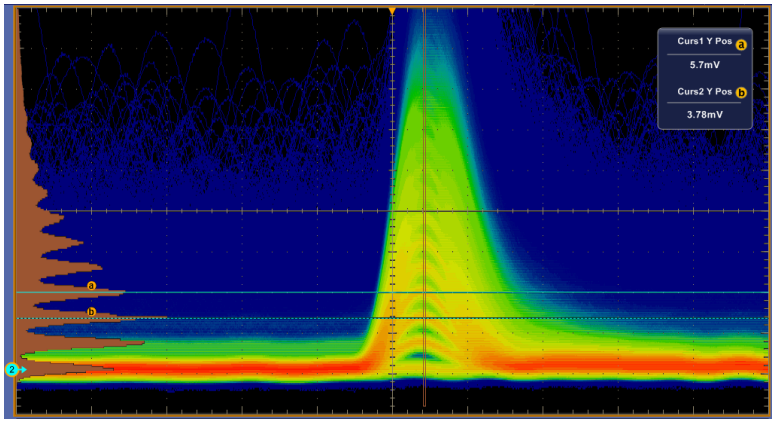

Fig. 32: Several few-photons overlying waveforms displayed on an oscilloscope screen-capture. The pulse height histogram is shown on the left of the screen, where the populations, due to different numbers of simultaneous photons, can be clearly distinguished.

A typical few-photons waveform in shown in Fig. 33(a). The oscilloscope can digitize analog waveforms with up to a 20 GHz sampling frequency and a 0.08 mV precision. A number of waveforms was saved in text files for an offline analysis. Due to the low amplitude of the analog

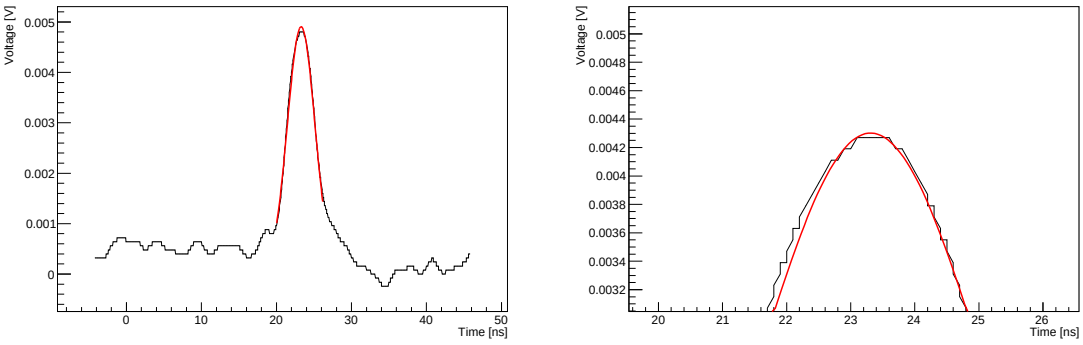

(a) (b)

Fig. 33: (a) Example of a digitized few-photons waveform, with gaussian fit around the maximum, detailed in (b).

signals, however, the sampling precision was not good enough to produce a sharp maximum, as shown in Fig. 33(b). Each digitized waveform was fitted to a gaussian in a fixed width interval around the maximum in order to identify their height, as shown in Fig. 33(a,b).
A limited fraction of the measured waveforms are broadened by noise detection, as can be seen in Fig. 34(a), resulting in a broadening of the waveform. Such spurious measurements are rejected with a cut on the gaussian fit σ, which was chosen as the discriminating parameter. Fig. 34(b) shows a distribution of such parameter: a narrow peak at lower σ values is recognizable. This peak is most likely formed by pure LED-generated photons waveforms, while the tail at higher σ is most likely due to spurious events. It was therefore chosen to reject waveforms with $\sigma > 2.1$.

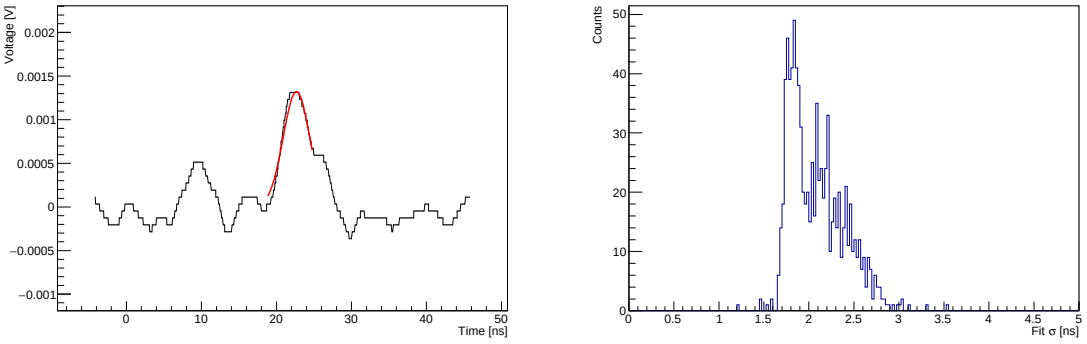

(a) (b)

Fig. 34: (a) Example of a spurious digitized few-photons waveform, clearly distorted by noise detection. (b) Distribution of the waveform core width, expressed as the σ of a gaussian fit to the waveform in the region around the peak.

The spectrum of waveform heights, obtained with the gaussian fit, is displayed in Fig. 35. The height spectrum presents equally spaced peaks, and each peak was associated to events with a defined number N of photons. The height spectrum resembles to a Poissonian distribution. The distribution of waveform heights in Fig. 35 is compared to the one obtained directly from the maximum of the digitized waveform before fitting (blue). In this case the amplitude values are discrete due to the coarse digitization.
The relation between peak centroids and the associated number of photons, shown in Fig. 36,

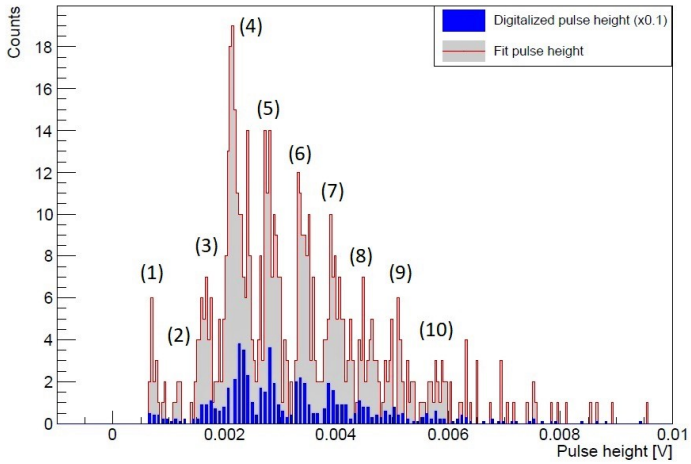

Fig. 35: Few-photons pulse height spectrum, obtained from digitized single waveforms by fitting the maximum (red), and considering the maximum sampled value without fitting (blue). The latter distribution is scaled down for sake of clarity.

N	min [mV]	max [mV]
1	0	0.35
2	0.45	0.9
3	1.0	1.4
4	1.5	2.1
5	2.25	2.6
6	2.8	3.2
7	3.35	3.8
8	3.95	4.3
9	4.5	4.9
10	5.1	5.6
11	5.7	6.0

Table 3: Pulse height intervals associated to different photon numbers N.

is approximately linear, with a (0.561 ± 0.008) mV/photon proportionality coefficient and a (0.02 ± 0.06) mV y-intercept. The linearity and the compatibility of the intercept with 0 confirm the correct association of each peak with the respective photon number. An interval was defined for each peak, so that every waveform, based on its maximum height, can be associated with a number of photons N. Waveforms non uniquely assignable, namely those whose height stands between two peaks, are discarded. The intervals ranges identifying each peak are listed in Tab. 3.

The average single-photon waveform can be obtained by averaging the few-photons signals, normalized by their respective N. The baseline, calculated as the average amplitude in the first 10 ns, was subtracted to each individual waveform. Mean single-photon waveforms, obtained separately from $N = 3$, 4, 6 and 8 are presented in Fig. 37(a), showing a good agreement between the different data sets, although the $N = 3$ waveform appears to be more affected by noise fluctuations. The mean single-photon waveform obtained from the entire sample is displayed in Fig. 37(b). The averaged single-photon waveform presents a raise time of about 3 ns and a decay time of about 5 ns. After the pulse, the waveform flattens to a negative value of amplitude, also referred to as *undershoot*. This behaviour is caused by the SiPM read-out

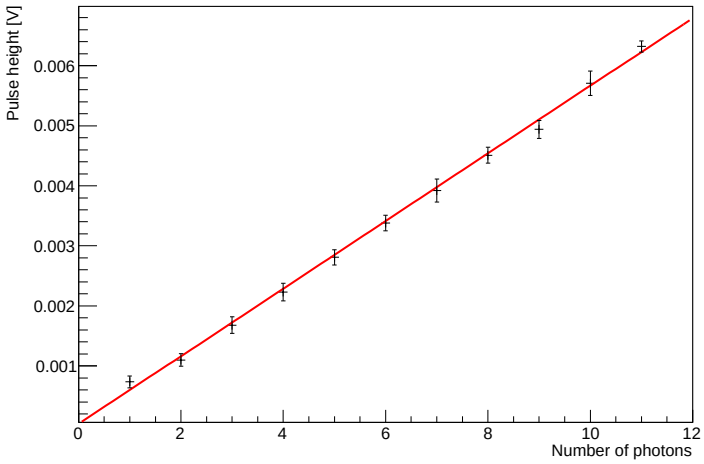

Fig. 36: Pulse height as a function of number of photons and linear fit.

electronics. The SiPM single cell signal presents the shape shown in Fig. 24, with a fast raise and a slow decrease. The SiPM read-out electronics, shown in Fig. 38, is designed to act as a *high-pass* filter, or *derivator*, to be able to transmit the fast signal raise. However the decreasing part of the SiPM cell signal is derivated into a negative constant value. In order to shorten the undershoot duration, different electronics are currently being studied for the next prototypes. The waveform was parametrized with a piecewise-defined custom function:

$$V_{\text{single}}(t) = \begin{cases} 0 & \text{if } \; t < t_0 \\ A \exp\left(-\frac{(t+\bar{t})^2}{2s^2}\right) & \text{if } \; t_0 \leq t \leq t_0 + t_1 \\ C + B \exp(-d\ t) & \text{if } \; t \geq t_0 + t_1 \end{cases} \tag{27}$$

where t_0 is the photon time of detection, $\bar{t} = 3.4435$ ns is the time at which the waveform reaches its maximum, $A = 0.8$ mV, $t_1 = 6.0253$ ns, $C = 0.0654$ mV, $B = 1762$ mV and $d = 0.352$ 1/ns are parameters fitted to reproduce the trend of the curve. This function was found empirically, in order to parametrize the waveform.

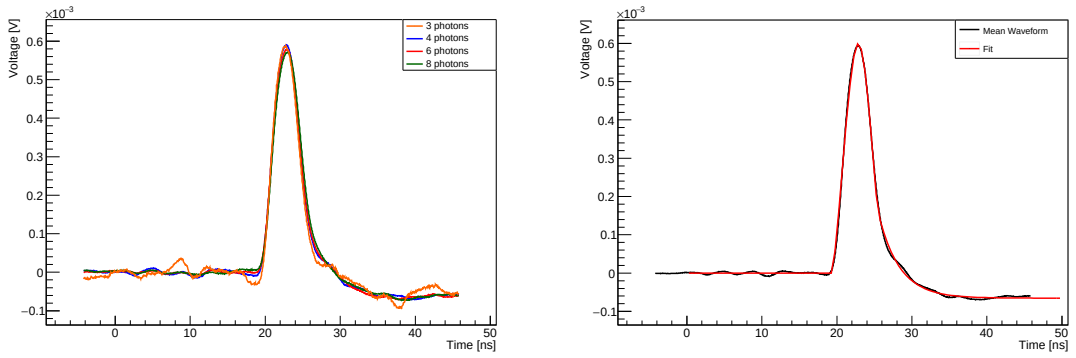

(a) (b)

Fig. 37: Single photon signals obtained from $N = 3,\ 4,\ 6$ and 8 data sets separately displayed (a); average single-photon signal from all the $N \geqslant 3$ few-photons signals, superimposed with the piecewise-defined function defined in Eq. (27).

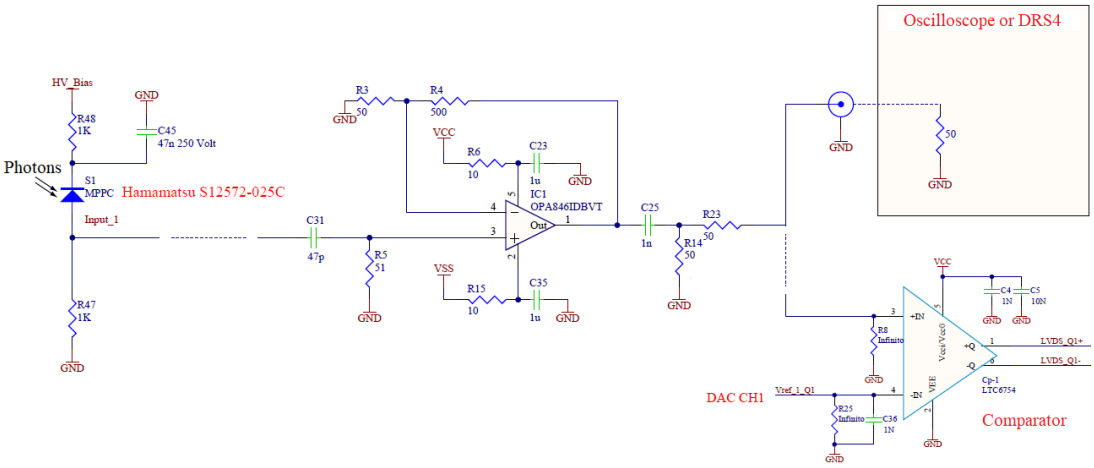

Fig. 38: Schematic of the current SiPM read-out electronics for the iMPACT calorimeter. Comparators implementation is foreseen.

5 Characterization with low energy protons

Preliminary tests with proton beam on candidate scintillators for the iMPACT calorimeter were conducted at the CN Van de Graaff 7 MV electrostatic accelerator, at INFN Laboratori Nazionali di Legnaro (LNL), on May 4^{th} and 5^{th}, 2017. The main goal of these tests was to characterize the response of a single PVT scintillating finger coupled to a SiPM.
The experimental setup is shown in Fig. 39: two PVT BC-420 fingers, highlighted in the picture, were held in place by a custom built metal support structure. One finger was wrapped with a teflon layer, while the other one was wrapped with an aluminum foil. Aluminum wrapping was considered, in a preliminary phase of the project, as an alternative to teflon, however the solution later was discarded due to the lower reflectivity of aluminum with respect to teflon. Therefore, only the teflon wrapped finger will be discussed from now on.
SiPM, also highlighted in the picture, were placed in contact with one of the fingers bases; the optical coupling was ensured by a layer of optical grease. The SiPM and its read-out electronics, shown in Fig. 40, were fastened to the support structure, in order to maintain the optical coupling during movimentation.

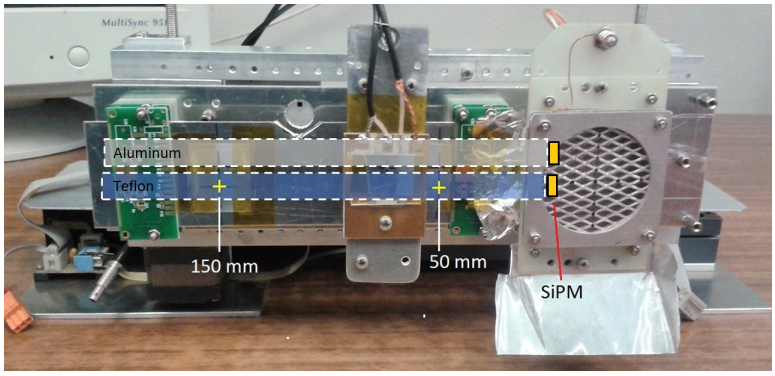

Fig. 39: Experimental setup used for the test beam at INFN-LNL CN accelerator. Teflon and aluminum wrapped fingers are highlighted.

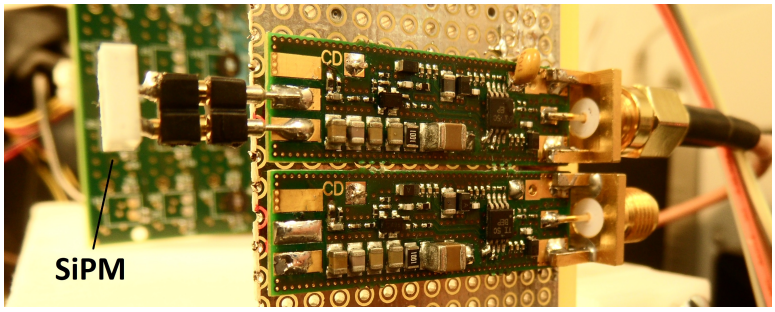

Fig. 40: Single SiPM front-end electronics prototype, used for the test beam at INFN-LNL CN accelerator.

The side of the finger facing the beam was covered with an aluminum plate, thick enough to stop the proton beam. Two holes were drilled into the aluminum plate at distance $d = 150$ mm ad $d = 50$ mm from the SiPM-side of the finger; the holes are indicated in Fig. 39 with yellow marks. A remotely controlled system was set up to cover alternatively one of the two holes. With this configuration protons could reach the finger only through the chosen hole, allowing to know the proton impact position on the finger.

The test was conducted using 3.5 MeV and 5 MeV protons; the energy resolution provided by the CN beam is approximately 0.1% (σ_E = 3.2 keV at 3.66 MeV) [77]. Protons at these energies are stopped by less than 35 cm of air, so the entire test was conducted in vacuum. Furthermore, two circular openings, with approximately 5 mm radius, corresponding to the holes in the aluminum layer, were opened in the teflon layer, which would have otherwise stopped the protons. Protons with such low energy penetrate only few micrometers inside the PVT volume, therefore at least 50% of the generated photons are lost, due to the lack of the reflecting teflon coating at the entrance window.
The setup for this early test was equipped with a provisional read-out, while the design of a dedicated electronics for the iMPACT calorimeter was still in progress. The provisional electronics single-photon response, shown in Fig. 41, was evaluated using a simplified version of the procedure presented in Sec. 31.

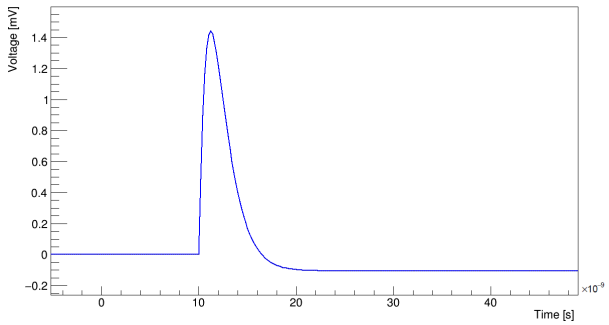

Fig. 41: Single-photon response of the SiPM and provisional read-out electronics used during the test at INFN-LNL CN accelerator, obtained from a simplified version of the procedure in Sec. 4.2.

The analog waveforms were digitized with the DRS4 Evaluation Board manufactured at the Paul Scherrer Institut (PSI). [78]. The board features four 50 Ω terminated input channels, with a 10 ns precision internal clock, an internal trigger with user-defined thresholds and the possibility of coincidence measurements over multiple channels. The DRS4 chip can sample with frequencies from 0.7 GSPS to 5 GSPS with 1024 sampling points each and 8-bit precision. A single digitized waveform is shown in Fig. 42. The signal presents an overall duration of about 40 ns, much longer than the 1.5 ns decay time declared by the scintillator manufacturer (Tab. 2). Such longer signal can be due to the presence of the teflon wrapping, reflecting photons multiple times before they reach the SiPM. Another reason can be the presence of a slow scintillation component in PVT, not reported in the manufacturer's data sheet [62, 63], or simply a different definition of the time constant.
The measurements also showed a non-expected time structure of the signal, with multiple fast ripples clearly visible. This behaviour was further investigated by computing the average waveform, in order to expose a possible regular time sub-structure, in which case the average waveform would present the same ripples. Instead, in the case of only statistical fluctuation, an averaging process would show a smooth waveform.
Given the short duration of the ripples, all waveforms need to be precisely time-aligned before averaging, to avoid possible time jitter given by the threshold-based trigger. The following procedure was therefore applied: each single waveform was individually interpolated with a custom function operatively defined as the sum of two exponentials describing the raise and the decay of the signal respectively:

$$V(t) = A\left[\exp\left(\frac{t_0 - t}{b}\right) - \exp\left(\frac{t_0 - t}{c}\right)\right] \quad ; \quad \text{for } t > t_0 \tag{28}$$

and 0 otherwise, where t_0, A, b, and c are parameters obtained from the fit. The parameter t_0

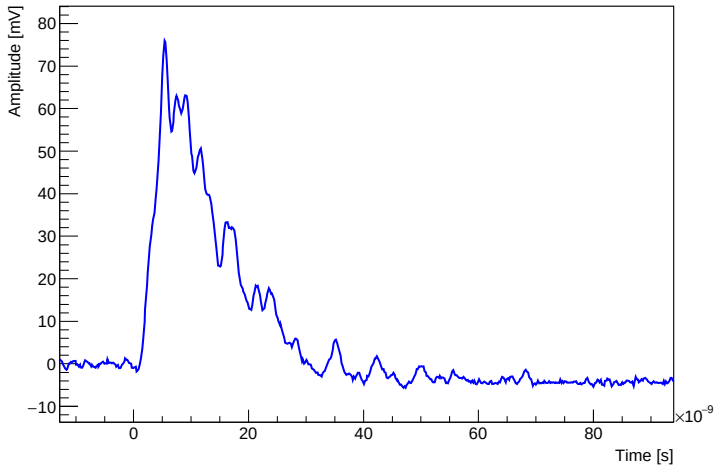

Fig. 42: Digitized single-proton event waveform, in the configuration $E = 5$ MeV and proton incident position $d = 150$ mm.

is the waveform starting time, and it correspond to the value for which $V(t_0) = 0$ in the raising part of the curve. An experimental digitized waveform, fitted with the function defined in (28), is shown in Fig. 43.

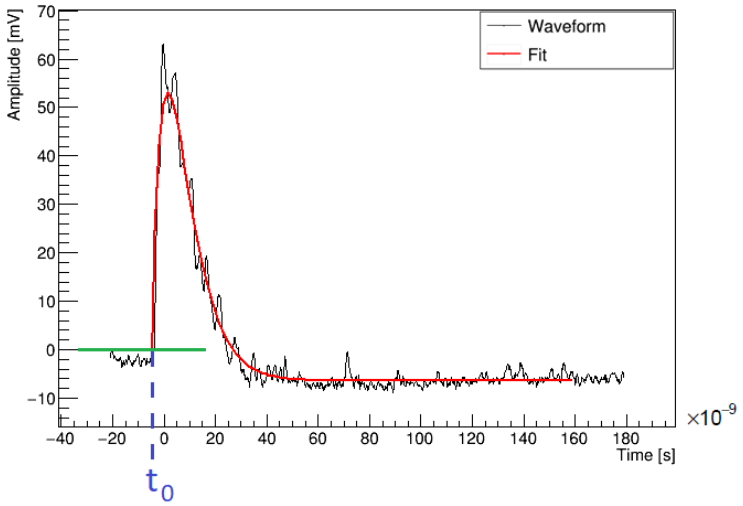

Fig. 43: Single waveform, fitted with the function (28). The waveform starting time t_0 is given by the value for which $V(t_0) = 0$ in the raising part of the curve. Configuration $E = 5$ MeV and $d = 150$ mm.

The waveforms were then aligned respect the starting time, shifting each one by t_0, and averaged. An average waveform, relative to the configuration $E = 5$ MeV and $d = 15$ cm, is shown in Fig. 44. The averaged waveform is smooth and does not present any fluctuation nor regular time structures: the ripples visible in a single signal are therefore due to the statistical nature of the photon detection and are then flattened by the averaging process.
To verify that the observed ripples are actually statistical fluctuations, the average number of detected photons in each signal was estimated, by dividing the integral of the average pulse

waveform, Fig. 44, for the integral of the single-photon signal, Fig. 41. The number of detected photons was found to be rather small, around 200 for a 5 MeV proton signal, and about 150 for 3.5 MeV. Statistical fluctuations in the small number of detected photons, caused most likely by the presence of the opening in the teflon around the proton hit position, are therefore compatible with the observed ripple.
The mean waveform reaches its maximum after about 10 ns, and returns to 0 in about 30 ns. The waveform, after the pulse, presents an undershoot of about 5 mV, caused by the readout electronics, as explained is Sec. 4.2. The decreasing region of the mean waveform was fitted with an exponential function, the decay time constant found was (12.3±0.2) ns.

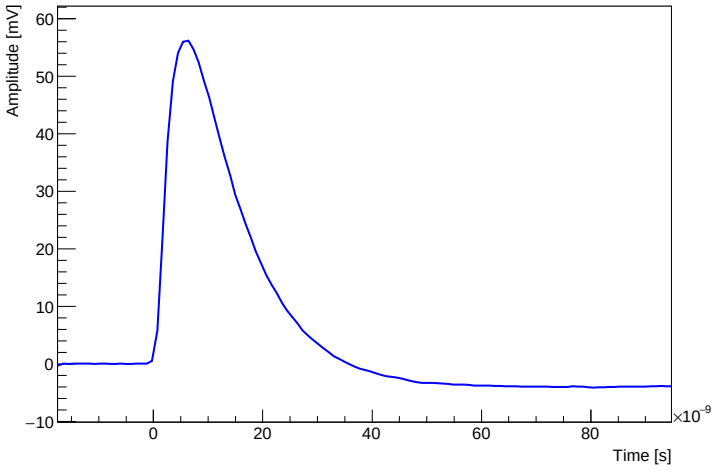

Fig. 44: Averaged experimental waveform; configuration $E = 5$ MeV and $d = 15$ cm.

The proton energy distribution is shown in Fig. 45 for the impact point $d = 50$ mm and in Fig. 46 for the impact point $d = 150$ mm. The energy deposited by each proton is derived from the value of the signal amplitude. Tab. 4 summarizes the test beam measurements. Energy distributions relative to $d = 150$ mm, i.e. protons detected farther from the SiPM surface, present in general between 15% and 20% lower pulses. In fact when scintillation photons are produced farther from the SiPM, they travel a longer path before detection, increasing the probability of absorption inside the material.
The distribution of the signal amplitude is rather wide, corresponding to an energy resolution of about 20% for both 3 and 5 MeV protons. This low energy resolution can be explained by the presence of the signal ripples, which increases the fluctuation of the waveform heights.

E [MeV]	d [mm]	**Pulse height [mV]**		
		Trigger: 5 mV	Trigger: 20 mV	Trigger: 35 mV
3.5	150	-	43.4 ± 8.2	-
3.5	50	-	47.3 ± 8.8	-
5.0	150	52.7 ± 14.8	53.0 ± 15.0	60.1 ± 11.0
5.0	50	64.9 ± 10.0	65.0 ± 9.0	66.1 ± 8.5

Table 4: CN test beam results: average pulse height for different beam energy E, position d and trigger.

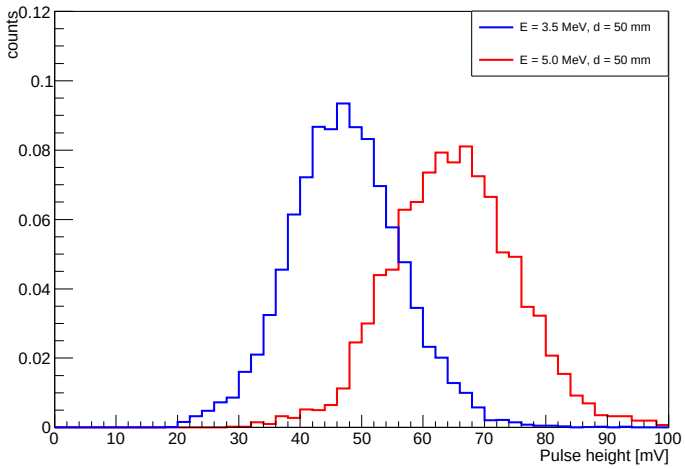

Fig. 45: Signal amplitude spectrum for 3.5 MeV and 5.0 MeV protons and $d = 50$ mm.

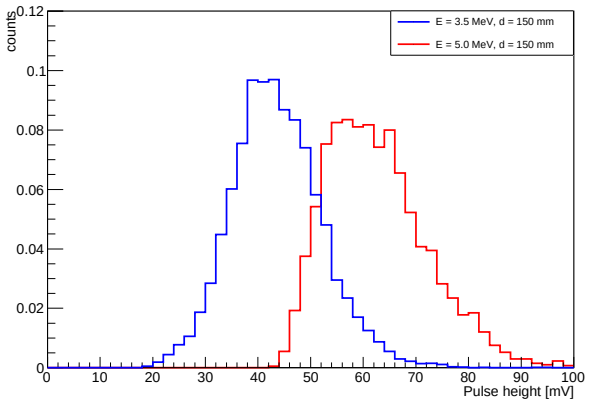

Fig. 46: Signal amplitude spectrum for 3.5 MeV and 5.0 MeV protons and $d = 150$ mm.

5.1 Simulation studies of the test beam setup

The CN test beam experimental setup was modelled in GATE as shown in Fig. 47. A single PVT finger, equipped with its SiPM according to Sec. 4 has been simulated, featuring a gaussian energy distribution centered on either proton energy $E = 3.5$ MeV or $E = 5$ MeV, and $\sigma_E/E = 1\%$, according to the CN beam parameters [77]. All four configurations corresponding to $E = 3.5$ MeV or $E = 5$ MeV and $d = 150$ mm or $d = 50$ mm were simulated. The entire apparatus was placed in vacuum. The teflon opening was defined as the contact surface between a cylinder with a 5 mm radius (green in Fig. 47), and the finger side. On the surface between the cylinder and the PVT, teflon reflective properties were removed. The cylinder was made of vacuum, therefore, presenting no physical differences from the rest of the *world*.

The measurements retrieved from the CN test beam were used to calibrate the simulation. It was chosen to proceed with the following approach: a single data set was arbitrarily adopted as reference for the simulation calibration, the $E = 5$ MeV and $d = 150$ mm, while the three remaining data sets were used as a test on its accuracy.

Firstly the PVT scintillation decay time constant has been changed to 12.3 ns, the value previously estimated from the averaged waveform in Fig. 44. A first simulation, maintaining the light yield value of 11136 photons/MeV, as in the BC-420 specifications, showed an average

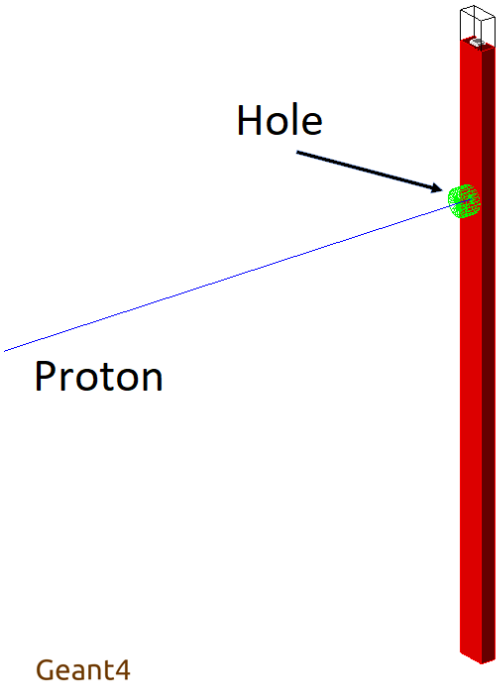

Fig. 47: INFN-LNL CN accelerator test beam setup modelled in GATE. The cylinder (green) represents the opening in the teflon wrapping.

number of detected photons around 1000 for each pulse, which is more than 5 times higher than the experimental number of detected photons. This discrepancy could be due to several factors, such as a non optimal reflectivity of the teflon wrapping and, more likely, a non ideal optical coupling between the SiPM and the PVT scintillator. To take into account this photon loss, the PVT light yield was reduced by a factor 5. A more rigorous approach would suggest to maintain the light yield and apply the reduction factor to the efficiency, however, decreasing the the photon production is, practically, not only equivalent but also more efficient in terms of computing resources.
The light yield parameter was then finely calibrated using the reference data set. Different simulations were performed changing the light yield parameter, and the simulated pulse height was compared to the experimental value. The simulated pulse height is shown, in Fig.48, as a function of the light yield; the red constant line marks the experimental value. The simulated data points were fitted with a linear function, the intersection of the fit and the experimental values was calculated to be 1891 photons/MeV. In the same way the Resolution Scale (RS) parameter, defined in Eq. 26, was estimated. However the heavy statistical fluctuations, already observed in the experimental waveform, Fig. 42, were also present in the simulated signals, as suggested by the considerable error bars in Fig. 48. The presence of this variability component, in addition to the PVT intrinsic resolution, described by the RS parameter, resulted in a difficult calibration of the latter. The RS was therefore only adjusted empirically to a value of 4; more refined tests on the energy resolution are planned in the future.
Such calibrated simulation was then validated by comparison to the measurements in the three remaining data sets. A single waveform generated from GATE data is compared with an experimental digitized signal, in Fig. 49. The simulated signal reproduces both the height and the duration of the experimental waveform. The number of detected photons is around 180, in good agreement with the experimental value of 200. Furthermore the ripple structure is similar in the simulated signal. This confirms the fact that ripples are a consequence of the low photon

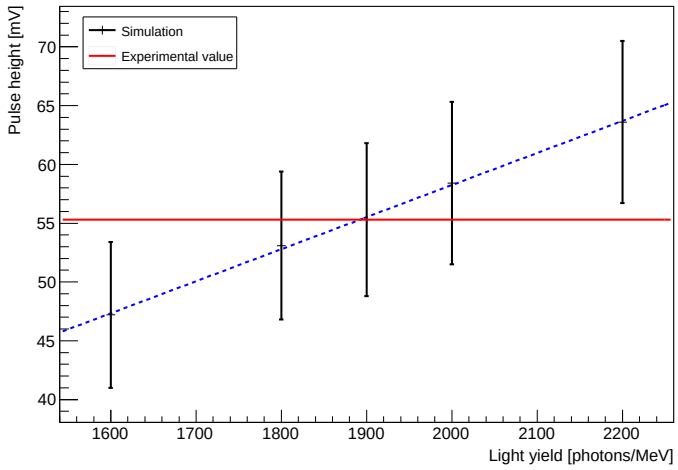

Fig. 48: Calibration of the light yield parameter to match the experimental pulse height value (red line), for the configuration $E = 5$ MeV, $d = 150$ mm.

statistics.

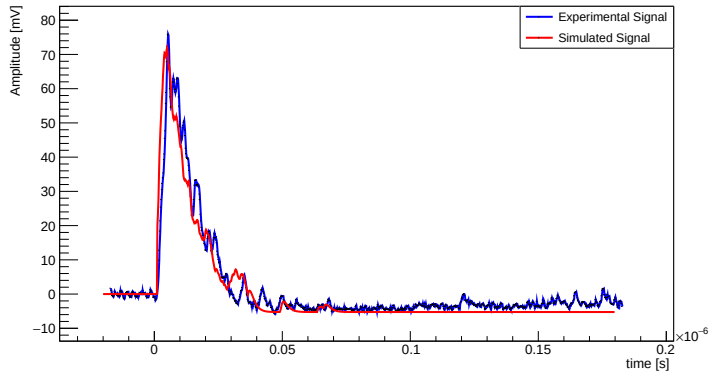

Fig. 49: Comparison between an experimental and a GATE simulated waveform, in the configuration $E = 5$ MeV and $d = 50$ mm.

A comparison of the experimental signal amplitude distribution to the simulated one is presented in Fig. 50. The simulated spectra peaks are, in both cases, well within the σ distance from the experimental peaks. Results from the simulation for all the four configurations are summarized in Tab. 5: simulated values are within 5% from the experimental values in all the cases except one. This shows the accuracy of the GATE simulation, able to reproduce not only signals from protons with different energies, but with also different impact point on the finger. For this reason this simulation tool is expected to be reliable also in reproducing the behaviour of larger and more complex configuration, ultimately a full scale calorimeter.

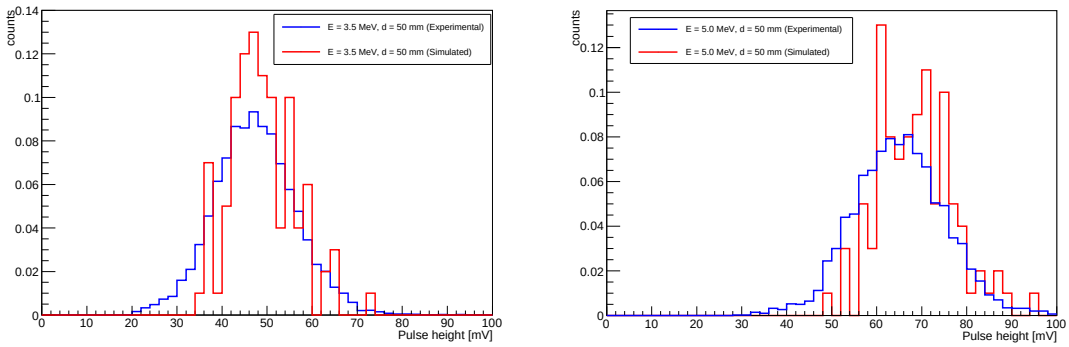

(a) (b)

Fig. 50: Comparison between experimental and simulated spectra for the configurations (a) $E = 3.5$ MeV and $d = 50$ mm.

E [MeV]	d [mm]	Pulse height [mV] Experimental	Simulated
3.5	150	43.4 ± 8.2	37.4 ± 5.2
3.5	50	47.3 ± 8.8	49.6 ± 6.9
5.0	150	55.1 ± 13.7	54.6 ± 6.8
5.0	50	65.0 ± 9.0	67.0 ± 8.6

Table 5: Comparison between experimental and simulated pulse height, for different configuration at INFN-LN CN accelerator test beam.

5.2 Signal duration vs length

The length of the PVT fingers was chosen to be 20 cm in a early stage of the iMPACT project, mainly based on geometrical arguments. However it was not proved if the length or the aspect ratio of the fingers have any significant repercussion on the duration of the signal, given the iMPACT requirement of a fast scanner. A set of simulations was performed in order to study the time response of a finger with varying length. The modelled setup is shown in Fig. 51. PVT fingers, with different length, from 10 to 25 cm, were simulated; a proton beam, with enough energy to pass through 5 mm of PVT, was positioned to impact at the center of the finger.

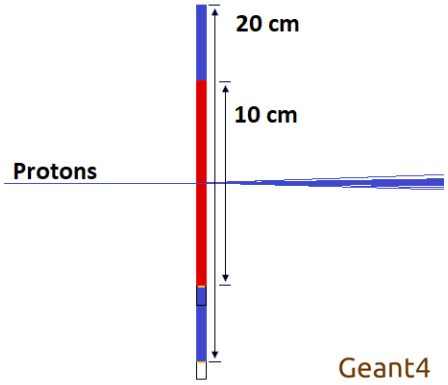

Fig. 51: Simulated setup with GATE, including fingers with different lengths. A proton beam impacts at the center of the fingers

In Fig. 52 (a) the time distribution of the detected photons, for different lengths, is shown; the distributions are averaged over 50 protons. The number of detected photons, as expected, decreases with longer fingers, with a factor 2 reduction going from a 10 cm to a 25 cm long finger. The time distribution, however, do not seem to change substantially with varying length, a part from a scale factor. Simulated analog signals, with different finger lengths, are shown in Fig. 52 (b); simulated signals are also averaged over 50 protons. Signals present, similarly to the time distribution, a lower amplitude for increasing finger lengths, while the duration remains almost unchanged.
The duration of the photon time spectrum Δt was defined as the difference between the time of the distribution maximum, $t_{\max}$ and the time at which the distribution height is 1/10 of the maximum value $t_{\max/10}$. The signal duration was instead defined as the difference between the maximum and the time at which the signal intercepts 0, $t(0)$. Results are presented in Tab. 6. The duration of the detection time distribution actually decreases slightly with shorter fingers. However the decrease is negligible, with only about 4 ns variation for a finger with a factor 2.5 shorter length. The time $t_{\max}$ is 1.3 ns longer in a 25 cm long finger with respect to a 10 cm long one, which is compatible with the fact that photons in PVT travel about 20 cm in a ns. The signals, instead, do not present any sensible variation in duration, most likely due to the electronics shaping process, which evens out the already small differences. The finger length does non sensibly change the analog signal duration, therefore this parameter can be adjusted accordingly to the assembling requirements.

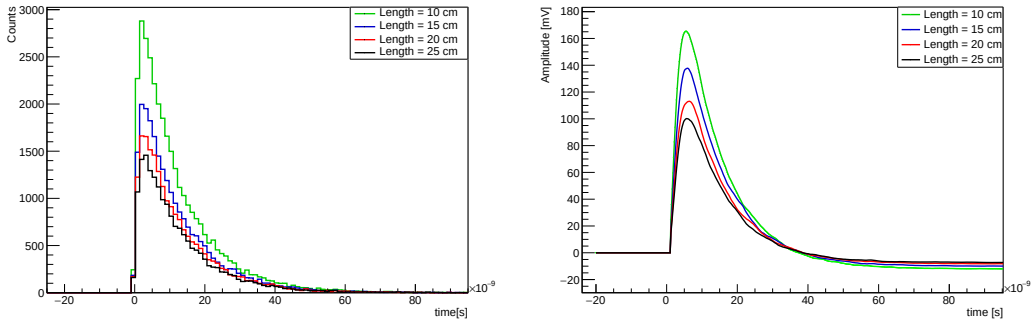

(a) (b)

Fig. 52: (a) Photon detection time spectrum for different finger lenght. (b) Simulated analog signal for different finger lenght.

Length	Time spectrum			Signal		
	$t_{\max}$ [ns]	$t_{\max/10}$ [ns]	Δt [ns]	$t_{\max}$ [ns]	$t(0)$ [ns]	Δt [ns]
10 cm	1.4	27.4	25.9	5.6	37.9	32.3
15 cm	2.3	28.2	25.9	5.6	38.7	33.1
20 cm	3.0	30.5	27.5	5.8	39.5	33.7
25 cm	2.7	32.2	29.7	6.4	38.9	32.5

Table 6: Simulated photon detection time spectrum and signals.

6 Studies with protons at hadron-therapy energies

A second characterization with proton beam was performed at the experimental line of the *Trento Institute for Fundamental and Applied Physics* (TIFPA) hosted at *Azienda Provinciale per i Servizi Sanitari* (APSS) proton-therapy facility [79] in Trento.
The Trento Proton Therapy facility started to be operative in October 2014. The facility is designed around an IBA Proteus 235 cyclotron, which can accelerate protons at energies between 70 MeV and 228 MeV, and includes two medical treatment rooms. More than 300 cases have been treated in the center until march 2017, in both adults and pediatric patients [79]. Outside clinical hours, the beam can be redirected towards an experimental room, administered by TIFPA, and dedicated to a wide range of scientific applications. The beam energy can be lowered down to 15 MeV, in the experimental line, by using appropriate degraders. The beam size is about 1 cm FWHM.

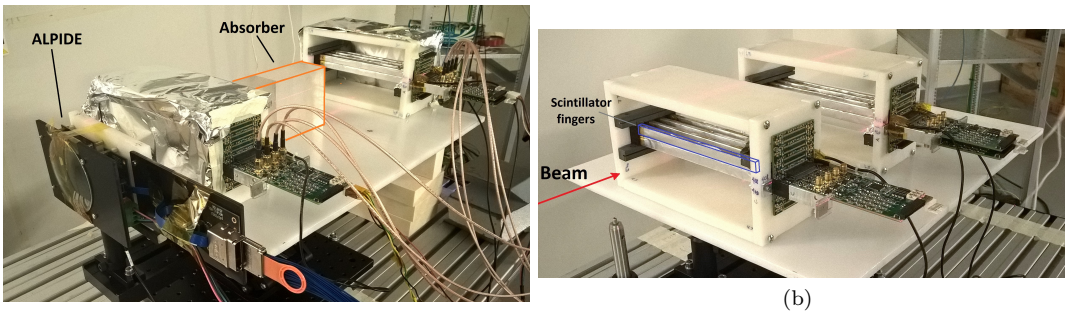

(a) (b)

Fig. 53: (a) Setup used for the test at the INFN-TIFPA APSS proton beam line. (b) Particular of the fingers arrangement.

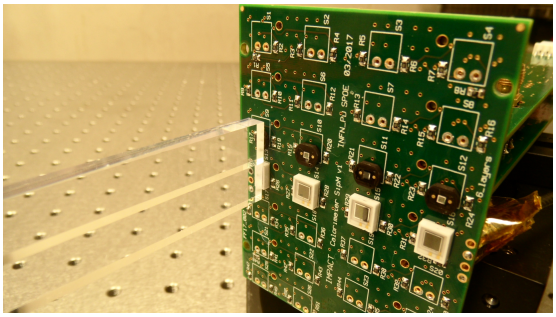

Fig. 54: Optical coupling between the SiPM and the scintillator finger.

A multiple-finger layout was studied in this test. The fingers were arranged in two identical units, as shown in Fig. 53, composing therefore a partial version of one module of the iMPACT calorimeter, as shown in Fig. 16. Each unit is composed by 8 fingers, aligned in 4 planes, their full DAQ including a SiPM, a read-out electronics and input-output board; the components were held in place by a plastic structure. The detail of the coupling between fingers and SiPM is shown in Fig. 54. PVT fingers were wrapped with a teflon layer and a protective aluminum foil, for a total aluminum thickness of about 800 µm. The fingers arranged in the top row included two BC-420 and six BC-408 as well as two different SiPM models and read-out electronics, for comparison tests. The entire lower row, instead, included 8 identical BC-408 fingers and 3 mm × 3 mm Hamamatsu S12572-025c SiPM with a read-out electronics that was, unlike the one used during the test at INFN-LNL CN accelerator, designed specifically for iMPACT;

the custom-made electronics single-photon response is displayed in Sec. 4.2. This version of the read-out electronics was designed to have a less steep rise with respect to the provisional one, in order to smooth the ripples that were present in the previous test beam, as shown in Fig. 42. The analog channels were digitized with two PSI DRS4 boards [78]. The acquisition triggers with a coincident signal in both the 1^{th} and 4^{th} fingers. An ALPIDE sensor, presented in Sec. 3.2, was positioned in front of the two calorimeter modules, as shown in Fig. 53, for an independent characterization. The setup also included a plexiglass absorber, shown in Fig. 53 (orange). The thickness of the absorber plus the 8 fingers, was calibrated, using also results from simulation, to be about 28 cm in order to stop 228 MeV protons. This setup is equivalent to the thickness the entire iMPACT calorimeter. The relative position of the calorimeter modules and the absorber could be modified in order to measure the response to protons in different configurations.

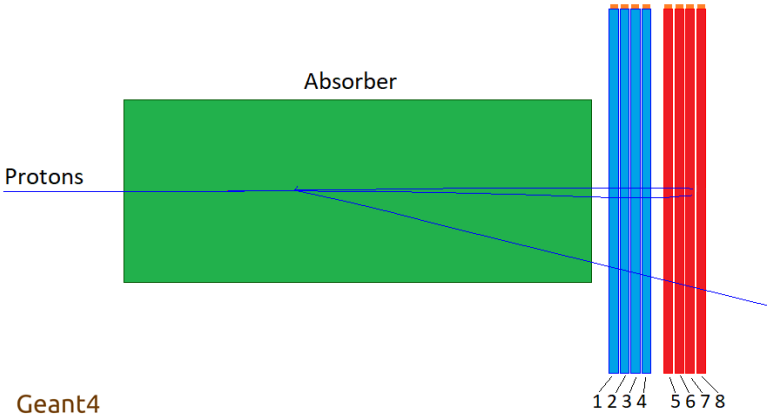

Fig. 55: Setup used for the test at the INFN-TIFPA APSS proton beam line, as modelled in GATE. Proton tracks stopping inside the fingers or scattering out are visible (blue)

The configuration with the absorber in front of 8 PVT fingers, which is shown using a GATE representation in Fig. 55, allows to observe the proton energy loss profile around the Bragg peak, to study the capability of the iMPACT calorimeter to measure the proton stopping position. The proton beam was set to 228 MeV.
Experimental signals in the 8 consecutive fingers, generated by the same proton event, are shown in Fig. 56; signals are time shifted with respect to each other for sake of clarity. The signal amplitudes outline the energy loss profile of the proton. The energy loss in the first 4 fingers is almost constant, corresponding to the plateau region of the Bragg curve; the energy deposition increases in the following fingers, reaching the maximum level in the 6^{th} finger; the proton then travels a short distance inside the 7^{th} one and stops; in fact, no signal is registered inside the last (8^{th}) finger. The finger inside which the proton comes at rest is therefore clearly recognizable; moreover it is possible to estimate the distance travelled inside such finger using the pulse height information from the previous ones. This represents a promising result for the iMPACT calorimeter development, showing the viability of a highly-segmented range-energy detector.
The signal pulse amplitudes averaged over multiple protons are shown in Fig. 57 for each finger. In this case the energy deposition profile is not as clear as the previous one. The maximum energy deposition takes place inside the 7^{th} finger, however the signal amplitudes in the first 4 or 5 fingers is compatible, within one standard deviation, with the peak. This can be due to the fact that a significant portion of the detected protons does not release their entire residual energy inside the fingers. In fact, fingers cover only 1 cm in the vertical direction, so protons passing through the first ones could deviate from a linear trajectory, enough to miss the

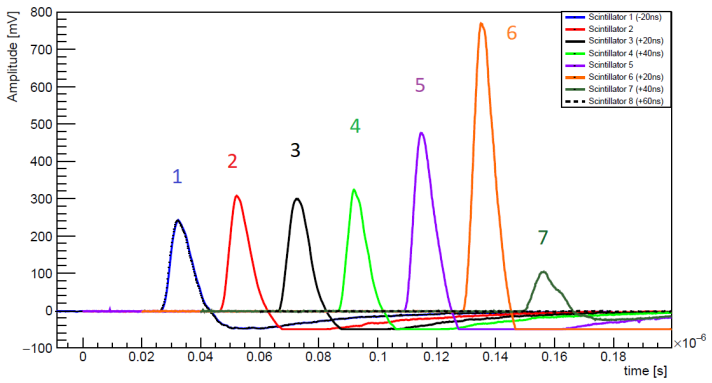

Fig. 56: Measured signals in the 8 fingers, from the same proton event. Signal waveforms are separated in time for sake of clarity.

following ones. This behaviour is shown in Fig. 58, where simulated proton tracks, leaving the scintillator volume before stopping, are displayed. These protons would release energy only in the first fingers, decreasing the peak height in Fig. 57. Moreover, protons near the end of their path, being slower, are more likely to be deflected at larger angles. Missing energy from protons scattering out of the fingers is not relevant in view of the complete iMPACT calorimeter, where the total absorbing volume will be large enough to contain also protons deviating from the straight path.

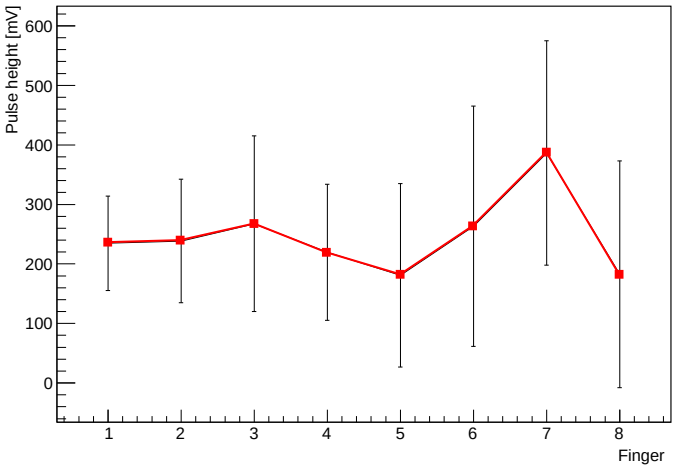

Fig. 57: Signal amplitudes averaged over multiple protons. The peak is lower than the expectations and measurements are affected by sizable uncertainties.

Information on the total deposited energy, can be derived from the sum of the pulse amplitudes in the 8 fingers, $V_{\text{tot}} = \sum_{i=1}^{8} V_i$, shown in Fig. 59. The V_{tot} spectrum appears to have a wide distribution, with a peak a lower values, meaning that protons are more likely to exit the fingers volume before releasing their entire energy. Protons stopping inside the fingers are only a limited fraction. A discrimination method has to be applied in order to reject protons scattering out of the fingers and to observe a clear integrated Bragg peak.
Both Fig. 56 and 57 ,as well as analogous information from simulated events, show that the 228 MeV proton Bragg peak is shared between the 6^{th} and the 7^{th} fingers, therefore a discrimination based on their signal amplitude, V_6 and V_7, is defined as follows. A scatter plot

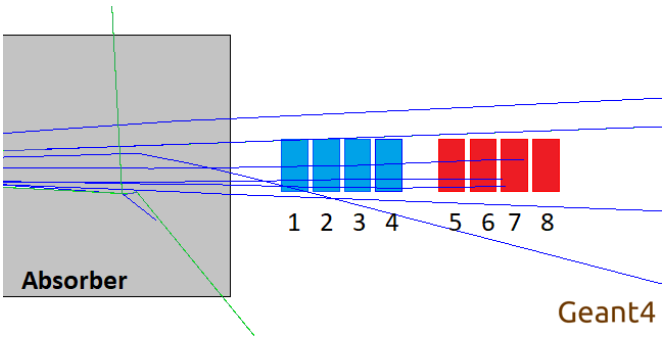

Fig. 58: Setup used for the test at the INFN-TIFPA APSS proton beam line, as modelled in GATE, with superimposed proton tracks (blue). Neutrons (green), produced by nuclear reactions, are visible.

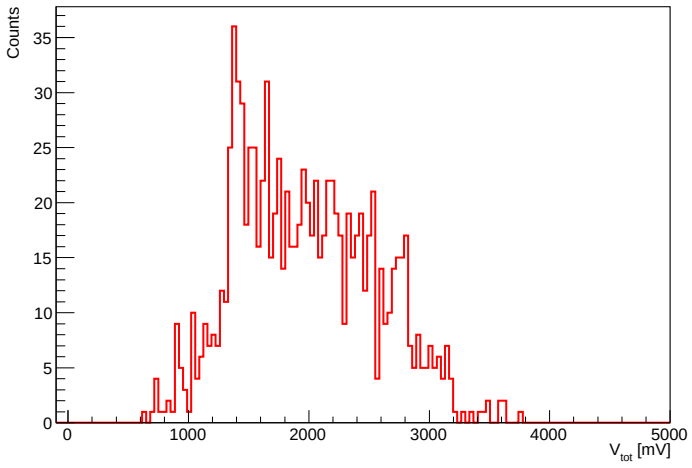

Fig. 59: Distribution of the sum of the signal amplitudes over the 8 fingers, V_{tot}.

displaying the parameter $r = (V_6 - V_7)/(V_6 + V_7)$ as a function on V_7 is shown in Fig. 60; different populations are recognizable. The acquisition displayed was obtained applying a threshold on the V_7 channel, for data reduction.
A number of events are distributed over an horizontal line at $r = -1$, corresponding to $V_6 \approx 0$. In these events the 7^{th} finger registered a signal, while the 6^{th} did not. This could be, most likely, caused by false ADC coincidences. The missing signal in the 6^{th} finger could also be due to protons that did not pass through the 6^{th} fingers and were then deviated towards the 7^{th} one by surrounding materials, for example the other fingers placed over the BC-408 row. Anyhow this type of event has to be rejected.
A fraction of events is distributed in a region around $r = 0$, which indicates a small difference between V_6 and V_7, slightly unbalanced towards $V_6 < V_7$. The majority of events in this population are located at low V_7, meaning both signals in the 6^{th} and 7^{th} finger are small. Most likely this region is given by protons that were scattered towards the fingers by surrounding materials, without passing through the absorber, so conserving a bigger fraction of their initial energy. In fact, the similar signal between the 6^{th} and the 7^{th}, suggest an energy deposition around the plateau region of the Bragg curve.
The last region is distributed from $r \approx 1$ and small signals in V_7, corresponding to $V_6 > V_7$, down to $r \approx 0$ at high values of V_7. This region is populated by protons whose energy was shared in variable proportions between the two fingers; most likely this area includes protons

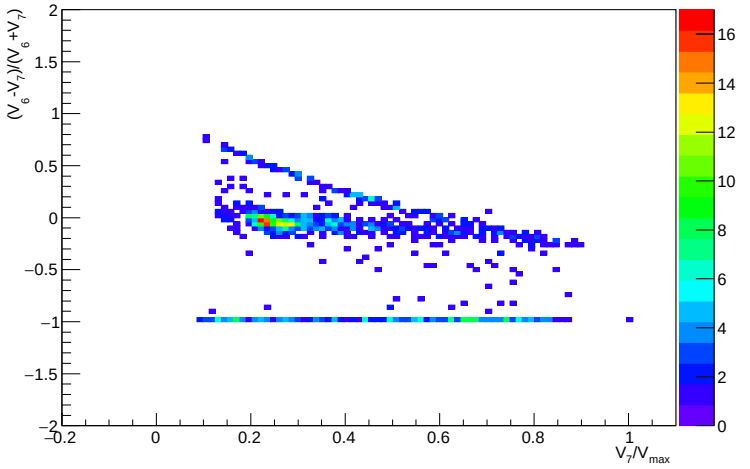

Fig. 60: Scatter plot from experimental data of the parameter $r = (V_6 - V_7)/(V_6 + V_7)$ as a function of V_7. V_7 is normalized to 1.

that stopped inside the fingers. A threshold on $V_6 + V_7$ is therefore expected to reject the first two population.

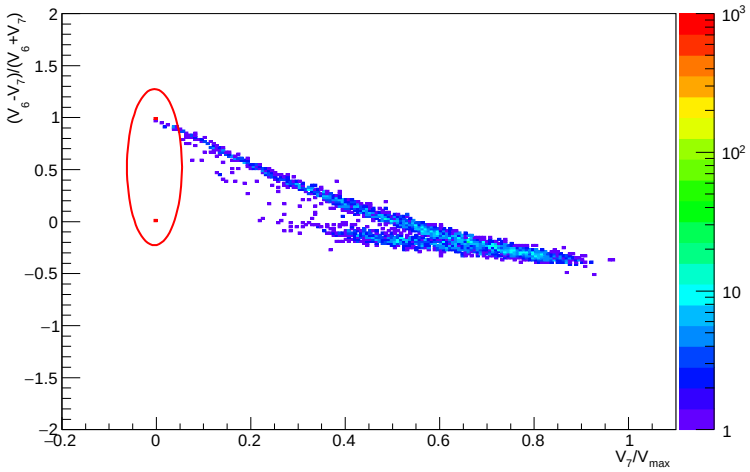

Fig. 61: Scatter plot from simulation data of the parameter $r = (V_6 - V_7)/(V_6 + V_7)$ as a function of V_7. V_7 is normalized to 1. The circled point at $V_7 = 0$ and $r = 1$ includes events with $V_7 = 0$ and $V_6 \neq 0$, while the point $V_7 = 0$ and $r = 0$ includes events with $V_7 = V_6 = 0$.

The experimental setup, modelled as in Fig. 55, was simulated with GATE. However the characterization of the BC-408 was still not complete, therefore the simulation was performed using the parameters calibrated with the BC-420 finger version. Moreover, the signal reconstruction algorithm was based on the preliminary version of the read-out electronics, shown in Fig. 41, in order to maintain a configuration that was proven to be stable and reliable, as shown in Sec 5.1. The results obtained with the simulation can not be compared quantitatively with the measurements, however they are expected to provide qualitatively comparable data. The proton source was defined as a monoenergetic 228 MeV pencil-beam.
Fig. 61 shows the distribution of simulated events as a function of r and V_7; V_7 is normalized to 1 in order to compare this plot with the experimental one. The plot was obtained applying the

same analysis tools, used for Fig. 60, to the simulated data. The simulated scatter plot presents two of the regions that appears in the experimental one. The oblique region from $r = 1$ and $V_7 \approx 0$ to $r = 0$, containing the protons that stopped inside the fingers, has a similar trend for both the experimental and simulated data.
The second population around $r \approx 0$ and weakly depending on V_7 appears as well, but only for higher V_7 values. In fact, this region, in the experimental conditions, included high-energy protons that were detected after being deviated by materials located in close proximity of the fingers. The simulation, however, does not include any surrounding material, therefore this population is not reproduced. The line at $r = -1$, caused by protons hitting the 7^{th} finger without intercepting the 6^{th} one is absent in the simulated data for the same reason.
A great fraction of the simulated events, more than 1000 out of 8000, are concentrated in two points at $V_7 = 0$, circled in Fig. 61. The point at $V_7 = 0$ and $r = 1$ corresponds to the case of a proton detected in the 6^{th} finger but not in the 7^{th} one. The point at $V_7 = 0$ and $r = 0$ corresponds instead to the case of no signal in either finger. These populations are concentrated in single points because the simulated output of a non-hit finger, unlike in any experimental setup, is exactly 0; future, more refined, simulations are planned to implement also noise effects. Both the cases featuring no signal in V_7 are absent in the experimental data set because of the threshold applied on the 7^{th} finger channel.

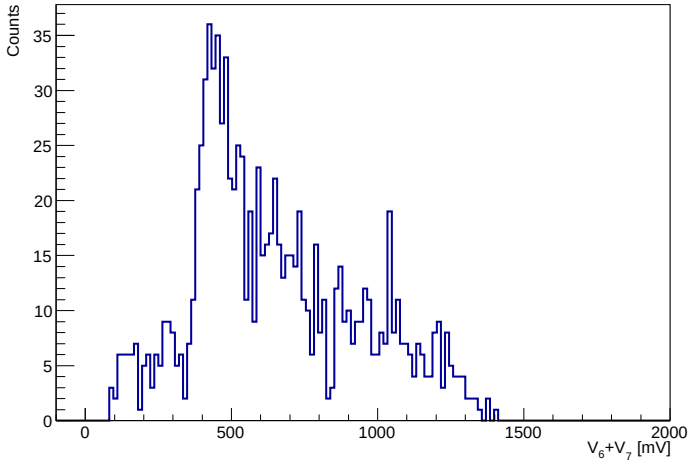

Fig. 62: Sum of pulse heights $V_6 + V_7$ distribution.

The threshold on $V_6 + V_7$ was applied in both the experimental and simulated data sets. The distribution of the experimental $V_6 + V_7$ values is shown in Fig. 62; the distribution presents a peak at lower values, similarly to the V_{tot} distribution in Fig. 59. It was chosen to reject events with $V_6 + V_7 < 1100$ mV, which represent the majority of the protons. The 1100 mV threshold corresponds to the 80% of the $V_6 + V_7$ parameter maximum value.
The scatter plot retrieved from experimental data, for $V_6 + V_7 > 1100$ mV, is shown in Fig. 63 (a), while the same plot retrieved from simulated data is shown in Fig. 63 (b). The level of the threshold on in the simulated data was calculated to be 80% of the $V_6 + V_7$ maximum value, the same fraction used for the experimental data set. In both the two plots the remaining region includes events with $V_7 \gtrsim V_6$ as well as a small fraction of events with $r > 0$, which includes protons that stopped inside the 7^{th} finger releasing, however, the biggest portion of their energy in the 6^{th} one, as the proton represented in Fig. 56.
The average pulse amplitude in each finger, with the threshold applied, is shown in Fig. 64, outlining the energy deposition profile. Results obtained from experimental and simulated data are to be compared only qualitatively. The experimental energy deposition profile is almost constant in the first four fingers and presents, as expected, a maximum in the 7^{th} finger, with

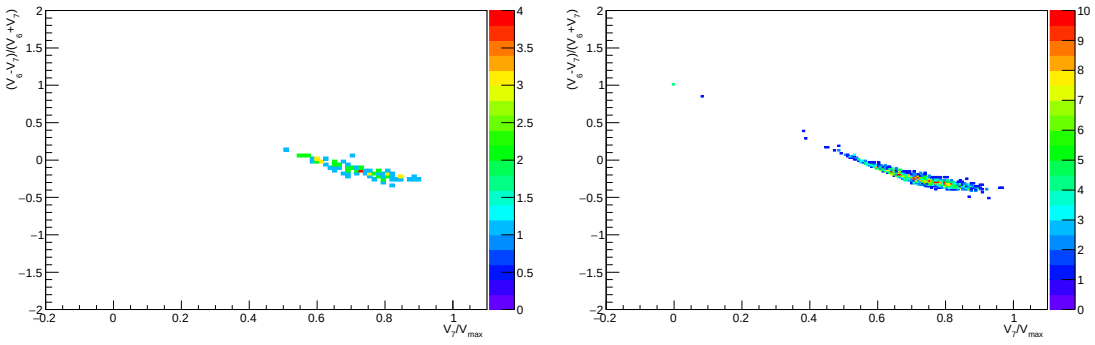

Fig. 63: Scatter plot of the parameter $(V_6 - V_7)/(V_6 + V_7)$ as a function of V_7, with a threshold on $V_6 + V_7$, from experimental data (a), and simulated data (b).

the signal in the 8$^{\text{th}}$ one dropping and reaching a value close to 0. The profile retrieved from simulated data shares the same behaviour, however, with a smoother trend. Additionally the 6$^{\text{th}}$ finger shows, in proportion, a higher energy deposition in the experimental data with respect to the simulation. This could indicate that protons in the experimental setup reach the last fingers with a slightly less energy, and stop at lower depths. Furthermore, the experimental values present generally higher errors with respect to the simulated ones, which can be caused by the better statistic in the simulation, an inaccurate calibration of the simulated energy resolution or an actual energy spread of the beam in the experimental conditions.

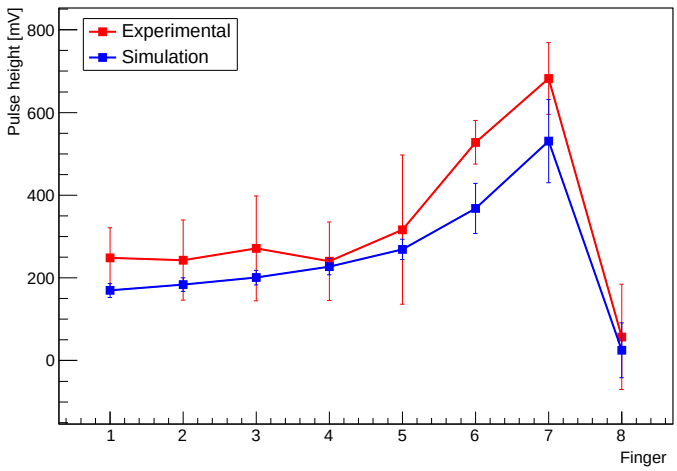

Fig. 64: Average signal amplitude, outlining the energy deposition profile along the 8 fingers, compared for experimental and simulated data.

Experimental energy spectra from different fingers, with the threshold on $V_6 + V_7$ applied, are presented in Fig. 65. The 1$^{\text{st}}$ and the 3$^{\text{rd}}$ finger spectra are, as expected, overlapped, being in the plateau region of the energy deposition profile. The 7$^{\text{th}}$ finger, where the highest average energy deposition takes place, shows a wider spectrum than the other ones, with a longer tail towards lower energies, which overlaps a portion of the 6$^{\text{th}}$ finger spectrum. The latter shows, instead, a narrower peak, distinguishable from the previous one. This clear separation between the finger in which the proton Bragg peak occurs, the previous one and those corresponding to the plateau region, indicates that the concept of an energy-range counter is applicable, even with

a lower sampling precision ADC. The plan to exploit a threshold-based digital discriminator for the iMPACT calorimeter read-out, as presented in Sec. 3.3, seems therefore feasible.

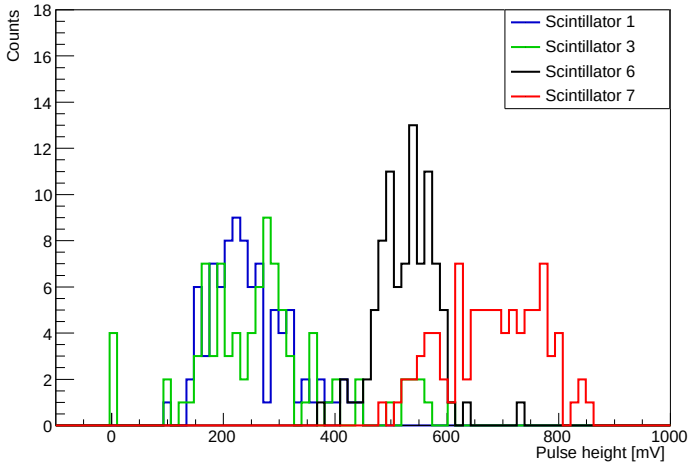

Fig. 65: Experimental signal amplitude spectrum from 1st (blue), 3rd (green), 6th (black) and 7th (red) fingers, with threshold on $V_6 + V_7$.

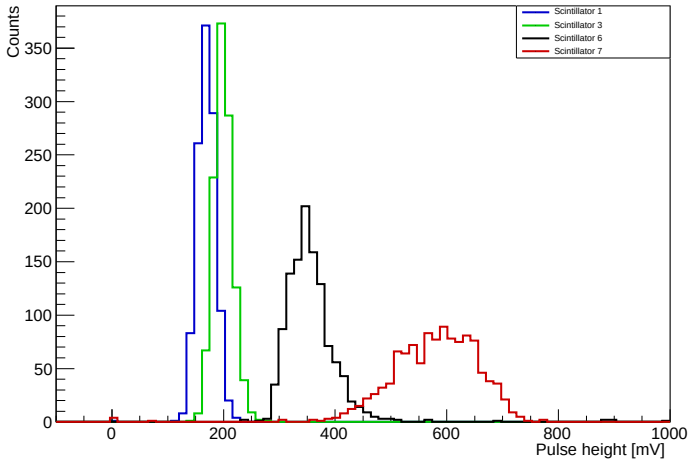

Fig. 66: Simulated signal amplitude from 1st (blue), 3rd (green), 6th (black) and 7th (red) fingers, with threshold on $V_6 + V_7$.

The simulated spectra from the 1st, 3rd, 6th and 7th fingers are shown in Fig. 66. The simulated spectra show comparable behaviour with the experimental one: the first fingers spectra are similarly overlapped, as well as the 7th finger which presents a wider distribution and a lower energies tail. However the 6th finger spectrum is translated towards lower energies, and further from the 7th finger spectrum. This confirms the assumption that in the experimental setup protons reach the last fingers with lower energies. The simulation, additionally, underestimates the energy distribution spread.
To confirm the accuracy of the cut, based on a threshold on $V_6 + V_7$, the spectrum of the sum of the pulse amplitudes V_{tot}, with the threshold applied, is shown in Fig. 67. The spectrum, compared to Fig 59, includes the events with a higher energy deposition, while the events in

the peak, that was present at lower energies in the distribution without the threshold applied, have been successfully rejected.

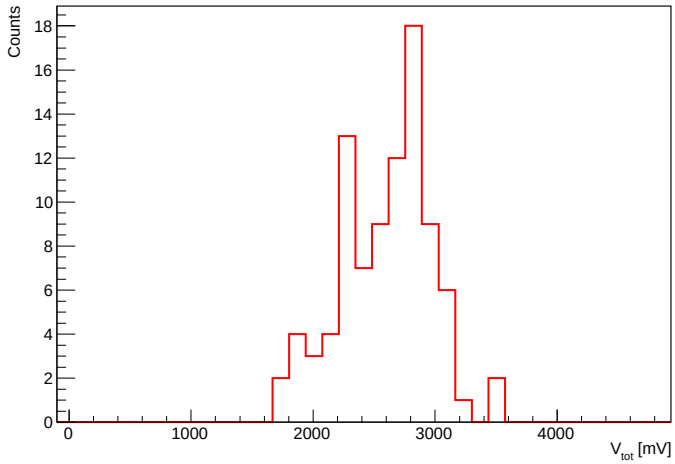

Fig. 67: Distribution of the sum of the signal amplitudes over the 8 fingers, V_{tot}, with threshold on $V_6 + V_7$.

The differences between the measurements and the simulation results could be due to the significant presence of materials in the experimental setup, which was not considered in the simulation. For example, the proton beam had to pass through the ALPIDE, along with the chip support and protective structures, before reaching the calorimeter modules; the presence of these materials could cause a broadening of the beam dimensions, defocussing, as well as widening and a lowering of its energy distribution. The higher energy spread of the proton beam, caused by MCS, could explain the wider energy distributions in the experimental case.
The presence of the additional PVT fingers on top of the 8 BC-408 could represent a relevant discrepancy between the experimental setup and the simulation, given the proximity between the elements. Additionally in the experimental setup, all the fingers were covered with an aluminum foil; the total aluminum thickness could also cause a non negligible energy loss to the protons, especially near the end of their path. Furthermore, some discrepancies can derive from inaccurate modelling of the absorber dimension, chemical composition and density. Further tests are however required in order to fully characterize BC-408 scintillator fingers, parameterizing their light yield as well as energy resolution and time response.
The analysis on the data collected during the test, with the calorimeter modules and the absorber in different configurations, as well as different beam energies, is still ongoing

6.1 Tracking system response evaluation

The ALPIDE sensor response was also analyzed, independently from the calorimeter, during the test at the INFN-TIFPA experimental beam line of the APSS proton-therapy facility. The main target of the tests on the sensor was to observe the dimension of the clusters, with varying beam energies and bias voltage applied. The analysis of these data is still ongoing and will not be presented here.
A quick demonstrative measurement was also performed during the beam time. A ballpoint pen was taped on the support structure of the ALPIDE, with the tip of the pen placed directly in front of the sentitive area of the detector, as shown in Fig 68. The proton beam energy was set to 70 MeV. The APLIDE sensor registered the hit position of the protons, after they interacted with the pen. The acquisition trigger was timed using an impulse generator. The ALPIDE trigger works with an inverse logic: the hold signal is at 0 V, while the trigger signal

is given by rectangular implulses with -800 mV amplitude and 2 µs duration; the acquisition frequency was set to 2 kHz. The bias voltage was set to 0. A hit map of the protons detection positions, displaying $6 \cdot 10^5$ events, is shown in Fig. 69. Each point represents a single 28 µm× 28 µm pixel, while the gray-scale indicates the number of hits in each pixel: a lighter color corresponds to a higher number of hits, while a darker color corresponds to a lower number of hits. The information on the proton hit position has not been correlated with information from the calorimeter on its energy, therefore the image produced can be considered as a simple *radiography* with protons. The shape of the internal components of the pen is outlined: the spring, the metallic tip and the plastic cap are visible. At the end of the metallic tip, a darker circle is noticeable, corresponding to the ballpoint of the pen, which has a higher density with respect to the metallic tip. In fact, protons scatter at higher angles in materials with higher densities, therefore, a darker *shadow* is visible behind denser objects. The lighter-gray area in the middle of the sensor is given by the higher intensity in the center of the proton beam, featuring about 1 cm FWHM. Fig. 69, however simple, shown the sensitivity of protons to different densities, a crucial feature for pCT. The figure, at the same time, illustrates the potential of a large area MAPS sensors in imaging applications.

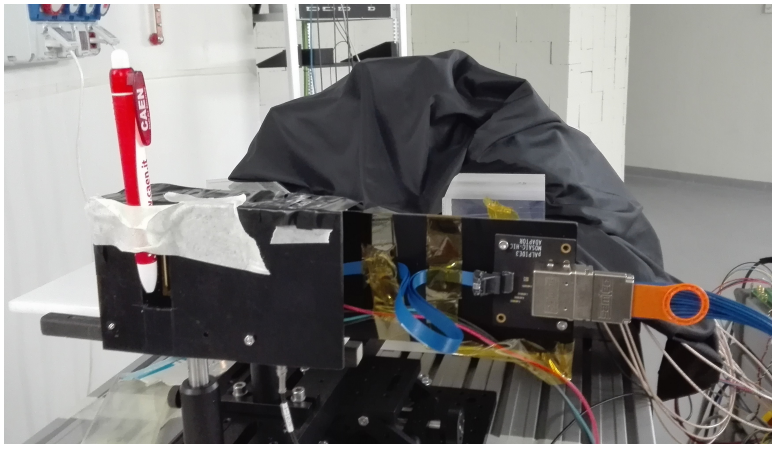

Fig. 68: Setup for the ballpoint pen image acquisition using the ALPIDE sensor.

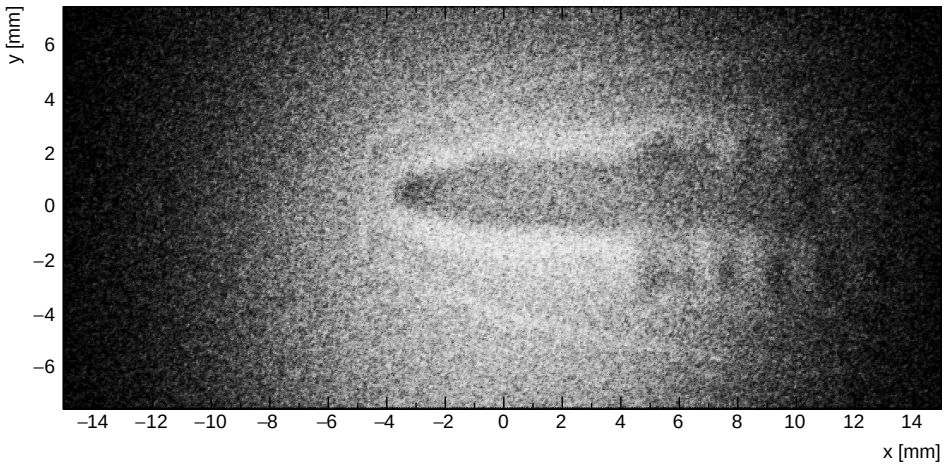

Fig. 69: Proton radiography of a ballpoint pen tip, as hits on the ALPIDE pixels.

7 Study of the linearity of the SiPM response

Each single APD cells that composes the SiPM sensitive surface features a dead time, or quenching time t_{quench}, as mentioned in Sec. 3.5, therefore additional photons reaching the same APD cell within t_{quench} after the detection of a photon, are lost. This feature is a source of non-linearity between the number of photons reaching the SiPM surface and the number of detected photons, particularly present in case of high photon fluxes. The number of detected photons is then proportional to the analog signal amplitude, as observed in Sec. 4.2.
The quenching time of the 3 mm × 3 mm Hamamatsu S12572-025c SiPM model used in the iMPACT calorimeter was assumed to be 100 ns, which is an average value among commercial SiPM models [68]. Once the quenching time will be measured, using the procedure displayed in Sec. 3.5, the results presented in this Section could be rescaled for the actual quenching time value.

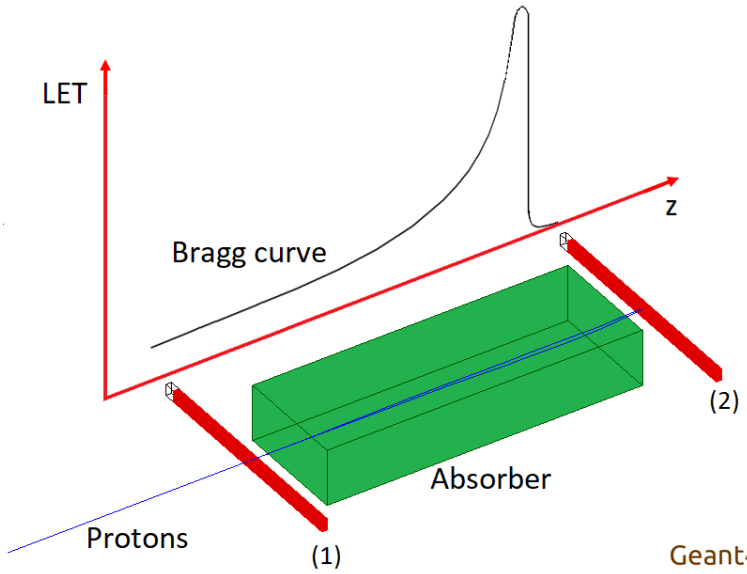

Fig. 70: Simulated configuration for the SiPM non-linearity study, with PVT fingers on the plateau (1) and on the peak (2) of the Bragg curve and a plexiglass absorber (green). Proton tracks are shown in blue.

A series of simulations were performed in order to quantify the fraction of photons lost due to the quenching time. On one hand this analysis quantifies the discrepancy between the simulation, which assumes $t_{\text{quench}} = 0$, and the experiment, while, on the other hand, it helps estimating the non-linearity between signal amplitude and deposited energy.
The simulated configuration, shown in Fig. 70, consists in a monoenergetic 230 MeV proton pencil beam and two PVT fingers; a plexiglass volume is placed between the two fingers. Protons pass through the first finger with the full 230 MeV energy, therefore the energy deposition inside this finger is at its minimum, in correspondence with the initial plateau region of the Bragg curve. Protons afterwards lose energy passing through the plexiglass absorber and only a fraction of them reach the second finger. The thickness of the absorber was calculated to be 28 cm, in order to make the protons stop inside the second finger, on average. Therefore the second finger placed in correspondence with the proton Bragg peak, where the maximum of the energy deposition takes place. The first and the second finger represent respectively the *best-case* scenario, where the minimum of scintillation photons is produced and multiple hits on the same APD cell are the least likely, and the *worst case* scenario, where the photon production is at its maximum and quenching time effects are the most impactful. The iMPACT calorimeter

operates between these two limits. The time duration of the simulated beam is set to 100 ns, as long as the assumed quenching time.
GATE, as mentioned in Sec. 4, provides the impact position of each detected photon, therefore it is possible to observe if an APD cell is hit more than once. An example of a two dimensional map of the photon hit positions on the 3 $mm \times 3$ mm SiPM surface is shown in Fig. 71, with each pixel corresponding to an APD cell. The number of detected photons, in the realistic case $t_{\text{quench}} = 100$ ns, is given by the number of hit cells, while the number of detected photons in the ideal case $t_{\text{quench}} = 0$ is given by the total number of hits. Simulations were performed with an increasing proton rate.

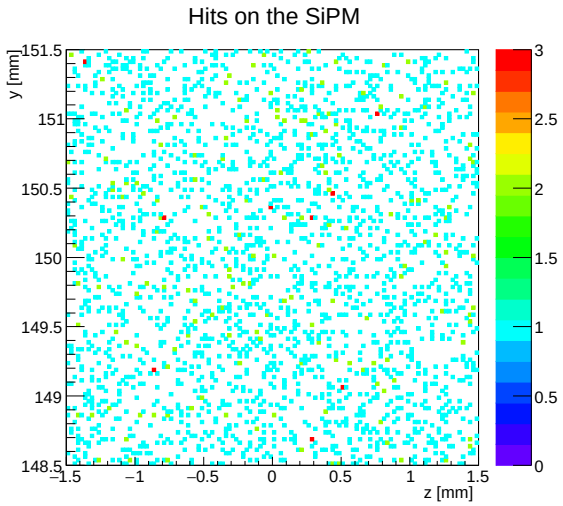

Fig. 71: Detected photon hit map on the SiPM surface.

The number of detected photons in the ideal, $t_{\text{quench}} = 0$, and realistic conditions, $t_{\text{quench}} = 100$ ns, are shown in Fig. 72, as a function of the proton rate, in the plateau region of the energy deposition profile (a) and in proximity of the Bragg peak (b); the errors are calculated as the standard deviation over several repeated simulations. The fraction of lost photons in the plateau is almost negligible, within the error bars, while in correspondence of the Bragg peak the fraction of lost photons reaches almost the 40% with 12 protons/100 ns, corresponding to a 120 MHz acquisition rate. In the latter condition the non-linearity between the number of photons reaching the SiPM and the number of detected photons, is also visible. The limited efficiency given by the quenching time can be calculated as the ratio between the number of detected photons in the realistic case $t_{\text{quench}} = 100$ ns and the ideal case $t_{\text{quench}} = 0$, and has to be multiplied for the the intrinsic SiPM efficiency, shown in Fig. 25, in order to obtain the total detection efficiency. The effect of t_{quench} on the efficiency is shown in Fig. 73. In the first finger, corresponding to the Bragg plateau, the efficiency remains higher than 90% with more than 10 protons per 100 ns, which corresponds to a 100 MHz rate, while the finger placed on the Bragg peak maintains an efficiency higher than 90% with less than 3 protons per 100 ns, equal to 30 MHz.
However the duration of the analog signal is about 50 ns, therefore the proton rate in a single finger can not be higher than 10 MHz, in order to avoid signal pileup.

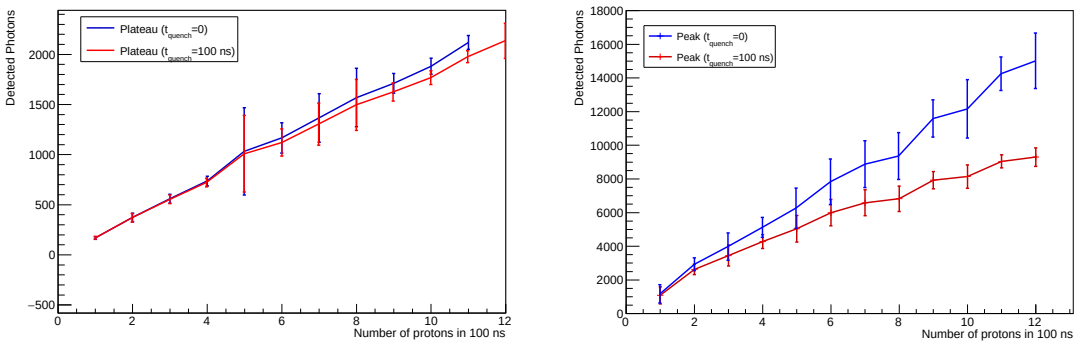

(a) (b)

Fig. 72: Number of detected photons, averaged over multiple simulations, as a function of the proton flux on a single PVT finger in the best case of null quenching time (blue) and in the worst case of $t_{\text{quench}} = 100$ ns (red). Protons at the plateau of the energy loss curve (a) are compared to protons at the Bragg peak (b)

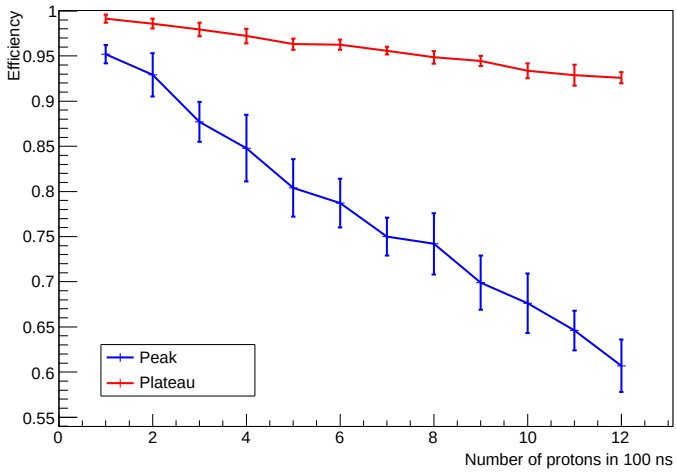

Fig. 73: Detection efficiency as a function of the number of protons is 100 ns.

8 Conclusions

Hadron-therapy is consolidating as a particularly effective technique for tumor treatment, in particular deep-seated neoplasms in brain or spinal tissues. The potential treatment precision of the technique, however, has not yet been fully exploited, due to the lack of an adequate pre-treatment imaging method capable of mapping the body tissue density with the resolution necessary to maximize the hadrons aiming accuracy. The Computed Proton Tomography (pCT) technology, by using particles with the same energy deposition profile as the ones used for the therapy as imaging probes, can generate such high-resolution density maps, which will maximize the treatment actual accuracy.
The iMPACT project foresees the construction of an extremely advanced pCT scanner, composed by a highly segmented energy-range calorimeter and a solid-state tracking system specifically designed to meet the requirements for a commercial and clinically viable system. In order to reach this goal, iMPACT plans to exploit some of the most recent technologies developed for particle detectors, such as the monolithic pixel sensor ALPIDE and massive use of Silicon Photomultipliers (SiPM).The resolution of the range calorimeter is competitive with the most precise proton tomography scanner prototypes currently under development around the world, while the acquisition rate is much higher thanks to its unique design.
A simulation tool has been developed to study the behaviour of the calorimeter and help choosing among different design options. The code simulates the entire process, from the primary proton energy deposition down to the analog signal at the SiPM output, and it is based on the pile-up of multiple single-photon pulses. It provides reliable results, both in simple test configurations as well as in more realistic, complex geometries. The simulation generates results compatible the actual measurements, for proton of different energy and impact position. The simulation code has been therefore validated and will play a key in guiding the full development of the iMPACT calorimeter.
A full characterization of the polyvinyl toluene BC-408 scintillator is planned to further improve the realism of the simulation. In particular, an accurate parametrization of the energy resolution of the designated detector appears essential for a correct evaluation of the accuracy achievable by the complete scanner. Additionally, simulation tests with a larger number of proton energies will be performed.
A way to improve the simulation accuracy is modelling the environment surrounding the detectors, starting from the materials in closer proximity to the fingers of the energy-range calorimeter. More refined simulations could include the tracker sensor layers in front of the calorimeter, actually reproducing the entire iMPACT scanner. More detailed characterization should also target the chosen SiPM model with the specific aim of better estimating its quenching time and high-signals response, parameters which allow a precise evaluation of the whole scanner efficiency respect the protons rate.
The iMPACT calorimeter early prototype has been extensively tested, first demonstrating that a full calorimeter is indeed feasible, and second validating the idea that a hybrid energy-range calorimeter is an effective component to realize a proton tomography scanner both fast and accurate. The next step is to assemble a full $8 \times 8 \times 32$ fingers stacks, in order to test the tracking capacities of the full calorimeter, and the maximum sustainable acquisition rate. Once the calorimeter will be commissioned, the effort will shift into correlating the calorimeter data with the tracker ones, to reach full proton trajectory determination.

9 Appendix

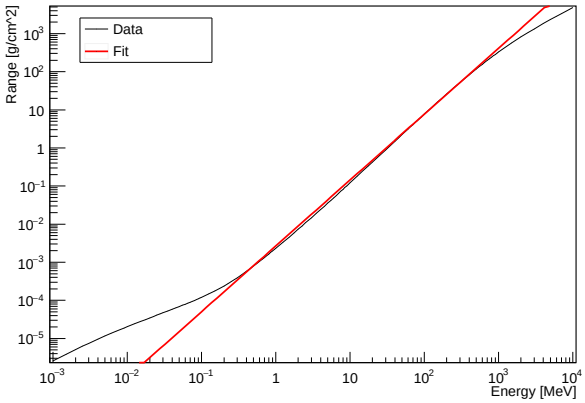

Fig. 74: Energy vs Range in polystirene-based scintillator NIST data [65] and fit with the Bragg-Kleeman rule Eq. (8) ($R = \alpha E^p$); fit performed in the $[1; 300]$ MeV range. ($\alpha = 0.00279 \pm 0.)00006$ g/cm^2, $p = 1.726 \pm 0.004$.

References

[1] A. Jemal, F. Bray, M. M. Center, J. Ferlay, E. Ward and D. Forman, *Global cancer statistics*, *CA: a cancer journal for clinicians* **61** (2011) 69–90.

[2] D. Schardt, T. Elsässer and D. Schulz-Ertner, *Heavy-ion tumor therapy: physical and radiobiological benefits*, *Reviews of Modern Physics* **82** (2010) 383.

[3] D. Cussol, *Hadron therapy*, in *École Joliot-Curie (30 years) "Physics at the femtometer scale"*, pp. 46–p, 2011.

[4] D. Campi, *Applicazioni mediche della fisica delle particelle*, *CERN* (2011) .

[5] R. R. Wilson, *Radiological use of fast protons*, *Radiology* **47** (1946) 487–491.

[6] C. A. Tobias and P. W. Todd, *Heavy charged particles in cancer therapy.*, *Nat. Cancer Inst. Monogr.* **24** (1967) 1–21.

[7] Particle Therapy Co-Operative Group. `https://www.ptcog.ch/index.php/facilities-in-operation`.

[8] Particle Therapy Co-Operative Group. `https://www.ptcog.ch/index.php/facilities-under-construction`.

[9] M. Mazzocco and D. Mengoni, *Radioattività e misure nucleari, (lecture notes)*, *Dipartimento di Fisica e Astronomia, Università degli studi di Padova* (2016/2017) .

[10] U. Linz and J. Alonso, *Laser-driven ion accelerators for tumor therapy revisited*, *Physical Review Accelerators and Beams* **19** (2016) 124802.

[11] E. J. Hall and A. J. Giaccia, *Radiobiology for the Radiologist*. Lippincott Williams & Wilkins, 2006.

[12] W. D. Newhauser and R. Zhang, *The physics of proton therapy*, *Physics in medicine and biology* **60** (2015) R155.

[13] H. Bethe, *Zur theorie des durchgangs schneller korpuskularstrahlen durch materie*, *Annalen der Physik* **397** (1930) 325–400.

[14] F. Bloch, *Zur bremsung rasch bewegter teilchen beim durchgang durch materie*, *Annalen der Physik* **408** (1933) 285–320.

[15] N. Bohr, *LX. On the decrease of velocity of swiftly moving electrified particles in passing through matter*, *The London, Edinburgh, and Dublin Philosophical Magazine and Journal of Science* **30** (1915) 581–612.

[16] W. H. Barkas, *Nuclear research emulsions*, *Academic Press* (1963) .

[17] W. H. Bragg and R. Kleeman, *XXXIX. On the α particles of radium, and their loss of range in passing through various atoms and molecules*, *The London, Edinburgh, and Dublin Philosophical Magazine and Journal of Science* **10** (1905) 318–340.

[18] H. Bethe and J. Ashkin, *Passage of Radiations through Matter,Experimental Nuclear Physics, Vol. 1, edited: E. Segre*, .

[19] W. Ulmer and E. Matsinos, *Theoretical methods for the calculation of Bragg curves and 3D distributions of proton beams*, *The European Physical Journal-Special Topics* **190** (2010) 1–81.

[20] P. Vavilov, *Ionization losses of high-energy heavy particles*, *Soviet Phys. JETP* **5** (1957) .

[21] L. D. Landau, *On the energy loss of fast particles by ionization*, *J. Phys.* **8** (1944) 201–205.

[22] N. Bohr, *Scattering and stopping of fission fragments*, *Physical Review* **58** (1940) 654.

[23] S. P. Ahlen, *Theoretical and experimental aspects of the energy loss of relativistic heavily ionizing particles*, *Reviews of Modern Physics* **52** (1980) 121.

[24] B. B. Rossi, *High-energy particles*. Prentice-Hall, 1952.

[25] J. F. Janni, *Proton Range-Energy Tables, 1 keV-10 GeV, Energy Loss, Range, Path Length, Time-of-Flight, Straggling, Multiple Scattering, and Nuclear Interaction Probability. Part I. For 63 Compounds*, *Atomic data and nuclear data tables* **27** (1982) 147.

[26] E. Rutherford, *LXXIX. The scattering of α and β particles by matter and the structure of the atom*, *The London, Edinburgh, and Dublin Philosophical Magazine and Journal of Science* **21** (1911) 669–688.

[27] G. Molière, *Theorie der streuung schneller geladener teilchen ii mehrfach-und vielfachstreuung*, *Zeitschrift für Naturforschung A* **3** (1948) 78–97.

[28] V. L. Highland, *Some practical remarks on multiple scattering*, *Nuclear Instruments and Methods* **129** (1975) 497–499.

[29] Y.-S. Tsai, *Pair production and bremsstrahlung of charged leptons*, *Reviews of Modern Physics* **46** (1974) 815.

[30] V. Giacometti, *Modelling and improvement of proton computed tomography*, Ph.D. thesis, University of Wollongong, 2016.

[31] A. Mustafa and D. F. Jackson, *The relation between X-ray CT numbers and charged particle stopping powers and its significance for radiotherapy treatment planning*, *Physics in Medicine and Biology* **28** (1983) 169.

[32] M. Yang, X. R. Zhu, P. C. Park, U. Titt, R. Mohan, G. Virshup et al., *Comprehensive analysis of proton range uncertainties related to patient stopping-power-ratio estimation using the stoichiometric calibration*, *Physics in medicine and biology* **57** (2012) 4095.

[33] A. M. Cormack, *Representation of a function by its line integrals, with some radiological applications*, *Journal of Applied Physics* **34** (1963) 2722–2727.

[34] A. M. Cormack, *Representation of a function by its line integrals, with some radiological applications. ii*, *Journal of Applied Physics* **35** (1964) 2908–2913.

[35] M. Goitein, *Three-dimensional density reconstruction from a series of two-dimensional projections*, *Nuclear Instruments and Methods* **101** (1972) 509–518.

[36] A. Cormack and A. Koehler, *Quantitative proton tomography: preliminary experiments*, *Physics in medicine and biology* **21** (1976) 560.

[37] U. Schneider, J. Besserer, P. Pemler, M. Dellert, M. Moosburger, E. Pedroni et al., *First proton radiography of an animal patient*, *Medical Physics* **31** (2004) 1046–1051.

[38] P. Zygmanski, K. P. Gall, M. S. Rabin and S. J. Rosenthal, *The measurement of proton stopping power using proton-cone-beam computed tomography*, *Physics in medicine and biology* **45** (2000) 511.

[39] J. Taylor, P. Allport, G. Casse, N. Smith, I. Tsurin, N. Allinson et al., *Proton tracking for medical imaging and dosimetry*, *Journal of Instrumentation* **10** (2015) C02015.

[40] R. Schulte, S. Penfold, J. Tafas and K. Schubert, *A maximum likelihood proton path formalism for application in proton computed tomography*, *Medical Physics* **35** (2008) 4849–4856.

[41] H.-W. Sadrozinski, R. Johnson, S. Macafee, A. Plumb, D. Steinberg, A. Zatserklyaniy et al., *Development of a head scanner for proton ct*, *Nuclear Instruments and Methods in Physics Research Section A: Accelerators, Spectrometers, Detectors and Associated Equipment* **699** (2013) 205–210.

[42] C. Civinini, D. Bonanno, M. Brianzi, M. Carpinelli, G. Cirrone, G. Cuttone et al., *Proton computed tomography: iterative image reconstruction and dose evaluation*, *Journal of Instrumentation* **12** (2017) C01034.

[43] R. Schulte, V. Bashkirov, T. Li, Z. Liang, K. Mueller, J. Heimann et al., *Conceptual design of a proton computed tomography system for applications in proton radiation therapy*, *IEEE Transactions on Nuclear Science* **51** (2004) 866–872.

[44] V. Bashkirov, R. Schulte, G. Coutrakon, B. Erdelyi, K. Wong, H. Sadrozinski et al., *Development of proton computed tomography for applications in proton therapy*, in *AIP Conference Proceedings*, vol. 1099, pp. 460–463, AIP, 2009.

[45] G. Poludniowski, N. Allinson and P. Evans, *Proton radiography and tomography with application to proton therapy*, *The British journal of radiology* **88** (2015) 20150134.

[46] G. P. Cirrone, G. Cuttone, G. Candiano, F. Di Rosa, S. L. Nigro, D. L. Presti et al., *Monte carlo studies of a proton computed tomography system*, *IEEE Transactions on Nuclear Science* **54** (2007) 1487–1491.

[47] D. L. Presti, D. Bonanno, F. Longhitano, C. Pugliatti, S. Aiello, G. Cirrone et al., *Design and characterization of a real time, large area, high spatial resolution particle tracker based on scintillating fibers*, *Biomed. Eng. Res.* **2** (2013) 159–174.

[48] Y. Saraya, T. Izumikawa, J. Goto, T. Kawasaki and T. Kimura, *Study of spatial resolution of proton computed tomography using a silicon strip detector*, *Nuclear Instruments and Methods in Physics Research Section A: Accelerators, Spectrometers, Detectors and Associated Equipment* **735** (2014) 485–489.

[49] S. Tanaka, T. Nishio, K. Matsushita, M. Tsuneda, S. Kabuki and M. Uesaka, *Development of proton ct imaging system using plastic scintillator and ccd camera*, *Physics in medicine and biology* **61** (2016) 4156.

[50] U. Schneider, E. Pedroni, M. Hartmann, J. Besserer and T. Lomax, *Spatial resolution of proton tomography: methods, initial phase space and object thickness*, *Zeitschrift für Medizinische Physik* **22** (2012) 100–108.

[51] T. E. Plautz, V. Bashkirov, V. Giacometti, R. Hurley, R. Johnson, P. Piersimoni et al., *An evaluation of spatial resolution of a prototype proton ct scanner*, *Medical physics* **43** (2016) 6291–6300.

[52] M. Hayat, *Cancer imaging: instrumentation and applications*, vol. 2. Academic Press, 2007.

[53] M. Goitein and M. Jermann, *The relative costs of proton and x-ray radiation therapy*, *Clinical Oncology* **15** (2003) S37–S50.

[54] First patient treated on Mevion's compact proton therapy system using in-room CT. http://medicalphysicsweb.org/cws/article/newsfeed/67619.

[55] European Research Council ,ERC Consolidator Grants 2014 results. https://erc.europa.eu/sites/default/files/document/file/erc_2014_cog_full_results_by_domain.pdf.

[56] L. Evans and P. Bryant, *LHC machine*, *Journal of instrumentation* **3** (2008) S08001.

[57] G. Apollinari, O. Brüning, T. Nakamoto and L. Rossi, *High Luminosity Large Hadron Collider HL-LHC*, Tech. Rep. CERN-2015-005, CERN, 2017.

[58] M. Mager, ALICE Collaboration et al., *ALPIDE, the Monolithic Active Pixel Sensor for the ALICE ITS upgrade*, *Nuclear Instruments and Methods in Physics Research Section A: Accelerators, Spectrometers, Detectors and Associated Equipment* **824** (2016) 434–438.

[59] Jazz Semiconductor. https://www.jazzsemi.com.

[60] J. W. Van Hoorne, *The upgrade of the ALICE Inner Tracking System-Status of the RD on monolithic silicon pixel sensors*, *PoS* (2014) 125.

[61] B. Abelev (ALICE Collaboration) et al., *Technical Design Report for the upgrade of the ALICE Inner Tracking Sistem*, *Journal of Physics G* **41** (2014) 087002.

[62] Saint-Gobain BC420 Data Sheet. http://www.crystals.saint-gobain.com/sites/imdf.crystals.com/files/documents/sgc-bc418-420-422-data-sheet_69699.pdf.

[63] Saint-Gobain BC408 Data Sheet. http://www.crystals.saint-gobain.com/sites/imdf.crystals.com/files/documents/sgc-bc400-404-408-412-416-data-sheet.pdf.

[64] V. Bashkirov, R. W. Schulte, R. Hurley, R. Johnson, H.-W. Sadrozinski, A. Zatserklyaniy et al., *Novel scintillation detector design and performance for proton radiography and computed tomography*, *Medical physics* **43** (2016) 664–674.

[65] NIST (National Institute of Standards and Technology) database. http://physics.nist.gov/PhysRefData/Star/Text/PSTAR.html.

[66] https://en.wikipedia.org/wiki/Triangular_distribution#cite_ref-KD_1-0.

[67] Hamamatsu SiPM Data sheet. http://www.hamamatsu.su/images/hamam/katalogi/mppc_kapd0002e.pdf.

[68] S. Seifert, H. T. Van Dam, J. Huizenga, R. Vinke, P. Dendooven, H. Lohner et al., *Simulation of silicon photomultiplier signals*, *IEEE Transactions on Nuclear Science* **56** (2009) 3726–3733.

[69] K. C. Burr and G.-C. Wang, *Scintillation detection using 3 mm× 3 mm silicon photomultipliers*, in *Nuclear Science Symposium Conference Record, 2007. NSS'07. IEEE*, vol. 2, pp. 975–982, IEEE, 2007.

[70] S. Jan, G. Santin, D. Strul, S. Staelens, K. Assie, D. Autret et al., *GATE: a simulation toolkit for PET and SPECT*, *Physics in medicine and biology* **49** (2004) 4543.

[71] S. Agostinelli, J. Allison, K. a. Amako, J. Apostolakis, H. Araujo, P. Arce et al., *Geant4—a simulation toolkit*, *Nuclear instruments and methods in physics research section A: Accelerators, Spectrometers, Detectors and Associated Equipment* **506** (2003) 250–303.

[72] A. Ferrari, P. R. Sala, A. Fasso and J. Ranft, *Fluka: A multi-particle transport code (program version 2005)*, Tech. Rep. CERN-2005-010, CERN, 2005.

[73] J. F. Ziegler, M. D. Ziegler and J. P. Biersack, *SRIM–The stopping and range of ions in matter (2010)*, *Nuclear Instruments and Methods in Physics Research Section B: Beam Interactions with Materials and Atoms* **268** (2010) 1818–1823.

[74] GATE Documentation.
`http://wiki.opengatecollaboration.org/index.php/Main_Page`.

[75] PicoQuant Pulsed LED Sources datasheet.
`https://www.picoquant.com/products/category/picosecond-pulsed-sources/pls-series-sub-nanosecond-pulsed-leds#description`.

[76] PicoQuant Pulsed Diode Laser Driver datasheet.
`https://www.picoquant.com/products/category/picosecond-pulsed-driver/pdl-800-b-picosecond-pulsed-diode-laser-driver#specification`.

[77] L. Silvestrin, D. Bisello, J. Esposito, P. Mastinu, G. Prete and J. Wyss, *SPES and the neutron facilities at Laboratori Nazionali di Legnaro*, *The European Physical Journal Plus* **131** (2016) 1–21.

[78] PSI DRS4 Evaluation Board.
`https://www.psi.ch/drs/DocumentationEN/manual_rev51.pdf`.

[79] F. Tommasino, M. Rovituso, S. Fabiano, S. Piffer, C. Manea, S. Lorentini et al., *Proton beam characterization in the experimental room of the Trento Proton Therapy facility*, *Nuclear Instruments and Methods in Physics Research A* **869** (2017) 15–20.